

Cluster Mass Reconstruction by a Weak Shear Field

Keiichi UMETSU ^{*)},
Masashi TADA ^{**)} and Toshifumi FUTAMASE ^{***)}

*Department of Astronomy, Graduate School of Science, Tohoku University,
Sendai 980-8578, Japan*

The tidal gravitational field of galaxy clusters causes a coherent distortion of the images of background sources. Since the distribution of image distortions, namely the shear field, traces the local gravitational potential of a deflector, it can be used to reconstruct the two-dimensional mass distribution of clusters of galaxies. Moreover, the shear field can provide unique information on the redshift distribution of high-redshift galaxies. In this review we summarize recently-developed parameter-free methods of cluster-mass reconstruction based on the shear field, and we apply a mass-reconstruction method to the cluster Abell 370 at redshift 0.375.

§1. Introduction

Clusters of galaxies are the most massive gravitational bound systems in the universe and therefore contain crucial information on the origin of structure formation and on cosmology.¹⁾⁻³⁾ For example, statistical studies of the cluster mass distribution and its evolution give us information on the distribution of dark matter and on the cosmological density parameter Ω_0 .

To this time, various methods have been used to determine the mass distributions in clusters of galaxies, such as: a dynamical method in which the velocity dispersion of member galaxies obtained from optical observations is used on the basis of the virial theorem,⁴⁾ and a method based on diffuse X-ray emission from the hot (\sim several keV) intra-cluster medium (ICM) that traces the gravitational potential of the cluster.⁵⁾ These two methods, however, are based on strong assumptions which are not fully justified. In applying the dynamical method, we must require that clusters are in virial equilibrium. However, this requirement is not always satisfied, because the typical dynamical time scale of a galaxy cluster is not much shorter than the Hubble time H_0^{-1} , at least for a high- Ω_0 universe, and the existence of substructures observed in some clusters indicate that they are not relaxed systems. Moreover, projection effects of substructures and the anisotropy of galaxy orbits in clusters may cause substantial errors in mass determinations by this method. On the other hand, X-ray analysis requires the assumption that the ICM is in hydrostatic equilibrium with the gravitational potential and also requires spherical symmetry for the mass profile of the cluster. These two methods are thus very sensitive to the physical and the dynamical state.

Another approach to determine the mass distribution of clusters is to make use

^{*)} E-mail address: keiichi@astr.tohoku.ac.jp

^{**)} E-mail address: tada@astr.tohoku.ac.jp

^{***)} E-mail address: tof@astr.tohoku.ac.jp

of gravitational lensing, which can in principle be used to determine the projected mass distribution of the lens object directly, independent of the physical state and the nature of the matter content. The light rays from background sources are deflected by clusters of galaxies, and the strength of the deflection depends on the total mass and the mass distribution of the deflector.

In the case of strong lensing, which occurs near the cluster core, the light-ray bending leads to the formation of *arcs* in cluster fields. If we assume spherical symmetry for the cluster mass distribution, the distance of an arc to the cluster center yields an estimate for the mass enclosed by a circle traced by the arc. An arc therefore places strong constraints on the cluster-mass distribution, especially in the central region of the cluster.

On the other hand, weakly-distorted images of background galaxies—so called *arclets*—can be observed to much larger angular separations from the cluster center, and thus they provide valuable information concerning cluster-mass distributions out to large radii.⁶⁾ Tyson, Valdes and Wenk⁷⁾ were the first to detect the weakly-distorted coherent images of galaxies behind two rich clusters. Kochanek⁸⁾ and Miralda-Escudé⁹⁾ attempted to fit parameterized mass profiles of the clusters to the observed distortion fields. Kneib et al.¹⁰⁾ placed strong constraints on the bimodal mass profile for the cluster Abell 370 using one giant luminous arc (hereafter referred to as GLA) and multiple images. Moreover, it has been shown that arc statistics are very sensitive to cosmological parameters, such as the cosmological constant Λ .^{11), 12)} Bonnet, Mellier and Fort¹³⁾ measured the coherent gravitational shear induced by the cluster Cl 0024+16 out to $3 h_{50}^{-1}$ Mpc, where h_{50} is the Hubble parameter in units of $50 \text{ km s}^{-1} \text{ Mpc}^{-1}$. It was first found by Kaiser and Squires¹⁴⁾ that the distortion field can be used for a parameter-free reconstruction of the two-dimensional mass density of a cluster in the weak-lensing regime. That is, the two-dimensional mass density of a deflector can be expressed as a convolution integral of the gravitational shear—which can be obtained from the image distortions of background galaxies in the weak-lensing limit—with a known kernel. The reconstruction formula derived by Kaiser and Squires was then generalized to include the strong-lensing regime^{15) - 17)} and modified to remove the artificial boundary effects,^{15), 18) - 21)} which arise in the resulting mass map obtained with the original Kaiser and Squires mass-reconstruction technique. These mass-reconstruction methods have been used to obtain the mass distributions of clusters in recent years (e.g., Refs. 22)~ 25).

In the present paper, we summarize the recent progress on the theoretical and the observational front in this field. There have been several reviews of this subject.^{26) - 28)} We shall try to be *self-contained* and *pedagogical* so that the reader can perform the cluster-mass reconstruction by reading this paper. The remainder of the paper is organized as follows: In § 2 we present basic equations and concepts of gravitational lensing. In § 3 we introduce the definition of the image shape, and describe how the local observables are related to the local properties of the lensing clusters. In Section § we review some mass-reconstruction schemes that are based solely on image distortions. As mentioned earlier, applications of the reconstruction formula derived by Kaiser and Squires to real data involve several difficulties. Here

we describe the difficulties which one encounters in applying the original reconstruction method to real clusters and how such difficulties can be overcome. Section 5 summarizes the observational studies of galaxy clusters based on the shear analysis. In § 6 we apply a mass-reconstruction method to the cluster Abell 370 to demonstrate the feasibility of the shear-based analysis. There we employ a new method to break the mass degeneracy associated with the mass reconstructions based solely on image shapes. Finally, we conclude with a summary in § 7.

§2. Gravitational Lensing

In this section we summarize the basic equations and concepts involved in gravitational lensing which we shall need later. For general treatments, see Refs. 29)-31).

2.1. Basic relations

The gravitational field of a deflector changes the source position $\vec{\beta}$ to the apparent position $\vec{\theta}$ according to the lens equation. Let $\Sigma(\vec{\theta})$ be the surface mass density of a deflector. The lens equation is written in terms of the two-dimensional effective lensing potential $\psi(\vec{\theta})$ in the form

$$\vec{\beta} = \vec{\theta} - \vec{\nabla}_{\theta}\psi(\vec{\theta}). \quad (2.1)$$

Here $\psi(\vec{\theta})$ satisfies the two-dimensional Poisson equation,

$$\Delta_{\theta}\psi(\vec{\theta}) = 2\kappa(\vec{\theta}), \quad (2.2)$$

where κ is the convergence defined by

$$\kappa(\vec{\theta}) := \frac{\Sigma(\vec{\theta})}{\Sigma_{\text{cr}}}, \quad (2.3)$$

with the critical surface-mass density

$$\Sigma_{\text{cr}} := \frac{c^2 D_s}{4\pi G D_d D_{\text{ds}}}. \quad (2.4)$$

Here D_d , D_s and D_{ds} are the angular-diameter distances from the observer to the deflector, from the observer to the source and from the deflector to the source, respectively. For a fixed lens redshift, we see that $\psi(\vec{\theta})$ depends on the source redshift through the distance ratio D_{ds}/D_s in Σ_{cr} .

Since $\psi(\vec{\theta})$ satisfies the two-dimensional Poisson equation (2.2), it can be written in terms of κ as

$$\psi(\vec{\theta}) = \frac{1}{\pi} \int d^2\theta' \ln |\vec{\theta} - \vec{\theta}'| \kappa(\vec{\theta}'). \quad (2.5)$$

We then introduce the components of the shear,

$$\gamma_1 := \frac{1}{2}(\psi_{,11} - \psi_{,22}) ; \quad \gamma_2 := \psi_{,12}, \quad (2.6)$$

where an index i ($i = 1, 2$) preceded by a comma denotes partial derivatives with respect to θ^i . It is useful to combine the shear components to define the complex shear,

$$\gamma := \gamma_1 + i\gamma_2 \equiv |\gamma| \exp(2i\phi). \quad (2.7)$$

We further define the *tangential shear* $\gamma_t(\vec{\theta}, \vec{\theta}')$ relative to the point $\vec{\theta}'$ by

$$\begin{aligned} \gamma_t(\vec{\theta}; \vec{\theta}') &:= -\left(\gamma_1(\vec{\theta}) \cos \left[2\varphi(\vec{\theta}, \vec{\theta}')\right] + \gamma_2(\vec{\theta}) \sin \left[2\varphi(\vec{\theta}, \vec{\theta}')\right]\right) \\ &= \Re \left[\gamma e^{-2i(\varphi + \frac{\pi}{2})}\right] = |\gamma| \cos \left[2\left(\phi - \varphi - \frac{\pi}{2}\right)\right], \end{aligned} \quad (2.8)$$

where $\Re(z)$ denotes the real part of a complex number z , and $\varphi(\vec{\theta}, \vec{\theta}')$ is defined by

$$\varphi(\vec{\theta}, \vec{\theta}') := \arctan \left(\frac{\theta_2 - \theta_2'}{\theta_1 - \theta_1'}\right). \quad (2.9)$$

From the definition, $\gamma(\vec{\theta})$ is a linear combination of the second derivatives of $\psi(\vec{\theta})$, so that the complex shear can be expressed by the convolutional integral of κ with a known kernel:

$$\gamma(\vec{\theta}) = \left(\frac{\partial_1^2 - \partial_2^2}{2} + i\partial_1\partial_2\right) \psi(\vec{\theta}) \quad (2.10)$$

$$= \frac{1}{\pi} \int d^2\theta' \mathcal{D}(\vec{\theta} - \vec{\theta}') \kappa(\vec{\theta}'). \quad (2.11)$$

Here $\partial_i := \partial/\partial\theta^i$ ($i = 1, 2$) and $\mathcal{D}(\vec{\theta})$ is the complex kernel,

$$\begin{aligned} \mathcal{D}(\vec{\theta}) &:= \left(\frac{\partial_1^2 - \partial_2^2}{2} + i\partial_1\partial_2\right) \ln |\vec{\theta}| \\ &= \frac{\theta_2^2 - \theta_1^2 - 2i\theta_1\theta_2}{|\vec{\theta}|^4} = \frac{-1}{(\theta_1 - i\theta_2)^2}. \end{aligned} \quad (2.12)$$

We note that there exists a *global* transformation that leaves $\gamma(\vec{\theta})$ invariant such that

$$\kappa(\vec{\theta}) \rightarrow \kappa(\vec{\theta}) + \kappa_0, \quad (2.13)$$

where κ_0 is an arbitrary constant. We see in § 4 that this degeneracy leads to an ambiguity in the mass distribution predicted by the reconstruction technique based solely on the shear field.

2.2. Magnification and image distortion

The local properties of the lens equation are described by its Jacobian matrix:

$$\mathcal{A}(\vec{\theta}) := \frac{\partial \vec{\beta}}{\partial \vec{\theta}} = \begin{pmatrix} 1 - \psi_{,11} & -\psi_{,12} \\ -\psi_{,12} & 1 - \psi_{,22} \end{pmatrix}. \quad (2.14)$$

From Eqs. (2.2), (2.6) and (2.7), the Jacobian matrix \mathcal{A} can be rewritten as

$$\begin{aligned} \mathcal{A}(\vec{\theta}) &= \begin{pmatrix} 1 - \kappa - \gamma_1 & -\gamma_2 \\ -\gamma_2 & 1 - \kappa + \gamma_1 \end{pmatrix} \\ &= (1 - \kappa) \begin{pmatrix} 1 & 0 \\ 0 & 1 \end{pmatrix} - |\gamma| \begin{pmatrix} \cos(2\phi) & \sin(2\phi) \\ \sin(2\phi) & -\cos(2\phi) \end{pmatrix}, \end{aligned} \quad (2.15)$$

and it has two eigenvalues

$$\Lambda_{\pm} := 1 - \kappa \pm |\gamma|. \quad (2.16)$$

We see from Eq. (2.15) that the convergence κ is the trace part, and the complex shear γ is the trace-free part of the Jacobian matrix $\mathcal{A}(\vec{\theta})$. The convergence term alone in Eq. (2.15) causes an isotropic focusing of the light ray, while the shear term induces anisotropy in the lens mapping. The quantity $|\gamma| = (\gamma_1^2 + \gamma_2^2)^{1/2}$ is the amplitude of the shear, and the phase ϕ is the position angle of the eigenvector that belongs to the eigenvalue $\Lambda_- = 1 - \kappa - |\gamma|$.

The magnification of an image is given by the convergence and the shear as follows:

$$\mu(\vec{\theta}) := \left| \det \left(\frac{\partial \vec{\theta}}{\partial \vec{\beta}} \right) \right| = \frac{1}{|\det \mathcal{A}|} = \frac{1}{|(1 - \kappa)^2 - |\gamma|^2|}. \quad (2.17)$$

The closed curves defined by

$$0 = \det \mathcal{A}(\vec{\theta}) \quad (2.18)$$

are called ‘critical curves’, on which the magnification diverges. The image plane is separated by critical curves; the regions where $\text{sign}(\det \mathcal{A}) = +1$ and -1 are called *even-* and *odd-parity* regions, respectively. An intrinsically-circular source is transformed to an ellipse with axis ratio (≤ 1) of $|\Lambda_-/\Lambda_+|$ for $\kappa < 1$ and $|\Lambda_+/\Lambda_-|$ for $\kappa \geq 1$ and magnified by the factor $\mu = 1/|\Lambda_- \Lambda_+|$. The gravitational distortion vanishes along the curve defined by $\kappa(\vec{\theta}) = 1$, which lies in the odd-parity region.

In particular, for a non-singular circularly-symmetric lens, there are two *circular* critical curves: the inner critical curve defined by $0 = \Lambda_+ = 1 - \kappa + |\gamma|$, and the outer critical curve defined by $0 = \Lambda_- = 1 - \kappa - |\gamma|$. Images close to the outer critical curve are elongated in the tangential direction, while images

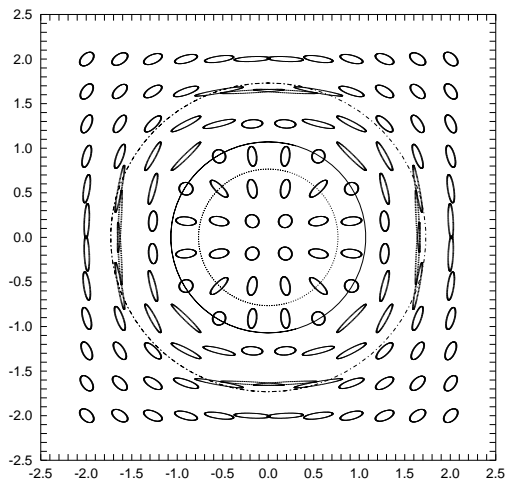


Fig. 1. Image-distortion field of intrinsically-circular sources for a non-singular circularly-symmetric lens. The dotted line represents the inner critical curve, where images are radially elongated. The dashed line represents the outer critical curve, where images are tangentially elongated. Image distortions vanish along the curve $\kappa = 1$ indicated by the solid line. The curve $\kappa = 1$ lies in the odd-parity region.

close to the inner critical curve are radially elongated (see Fig. 1). From these image properties, the outer and inner critical curves are called *tangential* and *radial*, respectively.

§3. Observables vs lensing properties

As stated in § 2.2, the tidal component of the gravitational field causes a coherent distortion of the images of background sources. Hence, the galaxy images observed through a cluster can be used to infer the lensing properties of the cluster. For this purpose, we must first quantify the shape of a galaxy image in terms of observable quantities. For an elliptically-shaped source, its shape and orientation can be defined in terms of the axis ratio and the position angle of the major axis, respectively. In this case, an appropriate image ellipticity can also be defined by them. However, observations of galaxies reveal quite irregular shapes which cannot be accurately approximated by a simple ellipse, and this irregularity leads to serious noise in measuring the shear field. We must, therefore, take account of the irregularity in quantifying a galaxy shape.

First, we define the center of a galaxy image by

$$\vec{\theta}_c := \frac{\int d^2\theta q[I(\vec{\theta})] \vec{\theta}}{\int d^2\theta q[I(\vec{\theta})]}, \quad (3.1)$$

where $I(\vec{\theta})$ is the surface-brightness distribution of the source galaxy, and $q(I)$ is a weight function, which we choose appropriately. For example, a possible choice for $q(I)$ may be the Heaviside step function $q(I) = H(I - I_{\text{th}})$, where I_{th} is a limiting surface brightness, and $H(x)$ is defined by

$$H(x) := \begin{cases} 1 & \text{for } x \geq 0 \\ 0 & \text{for } x < 0 \end{cases}. \quad (3.2)$$

In this case $\vec{\theta}_c$ is the center of the area enclosed by a threshold isophote $I(\vec{\theta}) = I_{\text{th}}$. For $q(I) = I$, $\vec{\theta}_c$ is the center of light. We then introduce the tensor of second brightness moments for each image:

$$Q_{ij} := \frac{\int d^2\theta q[I(\vec{\theta})] (\theta - \theta_c)_i (\theta - \theta_c)_j}{\int d^2\theta q[I(\vec{\theta})]}, \quad i, j \in \{1, 2\}. \quad (3.3)$$

With this definition, we can quantify the shape of a galaxy image using the complex ellipticity $\epsilon = \epsilon_1 + i\epsilon_2$:^{19), 32)}

$$\epsilon := \frac{Q_{11} - Q_{22} + 2iQ_{12}}{Q_{11} + Q_{22} + 2(Q_{11}Q_{22} - Q_{12}^2)^{1/2}} \equiv |\epsilon| e^{2i\phi}. \quad (3.4)$$

If galaxy images have elliptical isophotes with axis ratio $r (\leq 1)$, then the complex ellipticity is $\epsilon = (1 - r)/(1 + r) \exp(2i\phi)$, where the phase $\phi \in [0, \pi)$ is the position angle of the major axis.

Next, we consider the intrinsic (unlensed) surface-brightness distribution of the galaxy image $I_s(\vec{\beta})$, where the source position $\vec{\beta}$ is related to the image position $\vec{\theta}$ through the lens equation (2.1). Liouville's theorem tells us that gravitational lensing conserves surface brightness, and therefore we can set

$$I_s(\vec{\beta}) = I(\vec{\theta}). \quad (3.5)$$

We then define the tensor of second brightness moments Q_{sij} of an unlensed source as

$$Q_{sij} := \frac{\int d^2\beta q[I_s(\vec{\beta})] (\beta - \beta_c)_i (\beta - \beta_c)_j}{\int d^2\beta q[I_s(\vec{\beta})]}, \quad i, j \in \{1, 2\}, \quad (3.6)$$

where $\vec{\beta}_c$ is the angular position of the center of the unlensed source. If we assume that source images are smaller than the angular scale where the lensing properties change, then we can locally linearize the lens equation to obtain

$$(\beta - \beta_c)_i = \mathcal{A}_{ij}(\vec{\theta}_c) (\theta - \theta_c)^j. \quad (3.7)$$

From Eqs. (3.3), (3.6) and (3.7), we find that the tensors of second brightness moments of the source and image are related according to

$$Q_s = \mathcal{A}Q\mathcal{A}^T = \mathcal{A}Q\mathcal{A}, \quad (3.8)$$

where $\mathcal{A} \equiv \mathcal{A}(\vec{\theta}_c)$ is the Jacobian matrix of the lens equation at angular position $\vec{\theta}_c$. If we further define the complex ellipticities ϵ_s of the unlensed source in the same way as in Eq. (3.4), the transformation between source and image ellipticity is given by

$$\epsilon(\epsilon_s, g) = \begin{cases} (\epsilon_s + g)/(1 + g^*\epsilon_s) & \text{for } |g| \leq 1, \\ (1 + g\epsilon_s^*)/(\epsilon_s^* + g^*) & \text{for } |g| > 1, \end{cases} \quad (3.9)$$

where $g(\vec{\theta})$ is the *reduced shear* defined by

$$g := \gamma/(1 - \kappa), \quad (3.10)$$

and the asterisk denotes complex conjugation. Since $\det\mathcal{A} = (1 - \kappa)^2 (1 - |g|^2)$, the condition $|g| < 1$ ($|g| \geq 1$) is equivalent to the condition $\det\mathcal{A} > 0$ ($\det\mathcal{A} \leq 0$).

Hence, the lensing properties are related to the observable quantity ϵ only through the reduced shear g . In particular, the intrinsic ellipticity ϵ_s vanishes for circular sources, and thus we have

$$\epsilon = \begin{cases} g & \text{for } |g| \leq 1, \\ 1/g^* & \text{for } |g| > 1. \end{cases} \quad (3.11)$$

In general, on the other hand, source galaxies have intrinsic ellipticities, so that only one image gives us no information on the local gravitational field. We can, however, extract the local lensing properties from the observed distortion field by assuming that source galaxies are randomly oriented. If this assumption holds, that is, if

$\epsilon_s = |\epsilon_s| \exp(2i\phi)$ has a random phase ϕ , then the probability distribution function $p_{\epsilon_s}(\epsilon_s)$ of the source ellipticity ϵ_s in general takes the form

$$p_{\epsilon_s}(\epsilon_s) d^2\epsilon_s = p(|\epsilon_s|) |\epsilon_s| d|\epsilon_s| \frac{d\phi}{2\pi}, \quad (3.12)$$

where the function $p(|\epsilon_s|)$ is normalized so that $1 = \int_0^1 d|\epsilon_s| |\epsilon_s| p(|\epsilon_s|)$. It has been shown by Seitz and Schneider³²⁾ that the expectation value of the n -th moment ϵ^n is related to the reduced shear g through

$$\begin{aligned} \langle \epsilon^n \rangle_{\epsilon_s} &:= \int d^2\epsilon_s p_{\epsilon_s} \epsilon^n(\epsilon_s; g) \\ &= \int_0^1 d|\epsilon_s| |\epsilon_s| p(|\epsilon_s|) \oint \frac{d\phi}{2\pi} \epsilon^n(\epsilon_s; g) \\ &= \begin{cases} g^n & \text{for } |g| \leq 1, \\ 1/g^{*n} & \text{for } |g| > 1. \end{cases} \end{aligned} \quad (3.13)$$

Note that the expectation value $\langle \epsilon^n \rangle_{\epsilon_s}$ does not depend on the source-ellipticity distribution $p(|\epsilon_s|)$; if we adopt a different definition of the image ellipticity (e.g., Ref. 16)) its expectation value depends on its distribution.

In practice, however, we must replace the expectation value $\langle \epsilon \rangle_{\epsilon_s}$ with the average over a local ensemble of image ellipticities, $\bar{\epsilon}$:

$$\langle \epsilon \rangle_{\epsilon_s}(\vec{\theta}) \approx \bar{\epsilon}(\vec{\theta}), \quad (3.14)$$

where

$$\bar{\epsilon}^n(\vec{\theta}) := \frac{\sum_{i=1}^{N_{\text{gal}}} W(\vec{\theta} - \vec{\theta}_i) \epsilon^n(\vec{\theta}_i)}{\sum_{i=1}^{N_{\text{gal}}} W(\vec{\theta} - \vec{\theta}_i)}. \quad (3.15)$$

Here N_{gal} is the number of galaxy images, and $\vec{\theta}_i$ is the angular position of the i -th galaxy ($i = 1, 2, \dots, N$) defined by Eq. (3.1), and $W(\vec{\theta})$ is the weight function

$$W(\vec{\theta}) = \exp\left(-\frac{|\vec{\theta}|^2}{\Delta\theta^2}\right) \quad (3.16)$$

with smoothing scale $\Delta\theta$. This scale must be small enough so that the lensing properties can be assumed constant over the effective smoothing disk of area $\sim \pi\Delta\theta^2$ but large enough so that the smoothing disk contains a sufficient number of galaxies to suppress the random noise.^{17), 20)}

We can thus make use of the smoothed ellipticity field $\bar{\epsilon}(\vec{\theta})$ as a direct estimator for $g(\vec{\theta})$ or $1/g^*(\vec{\theta})$. In the case of weak lensing ($\kappa \ll 1$ and $|\gamma| \ll 1$, i.e., $|g| \ll 1$), we have

$$\gamma \approx g \approx \bar{\epsilon}. \quad (3.17)$$

In this limit, the shear γ is a direct observable.

§4. Cluster mass reconstruction by weak shear field

In this section we review several cluster-inversion methods based on the shear analysis. The point of this study is that the two-dimensional mass distribution of a cluster can be directly obtained only from the observed shear field, and that we need not assume *a priori* a mass profile of a cluster. In § 4.1 we review the original mass-reconstruction method developed by Kaiser and Squires¹⁴⁾ and summarize several difficulties we encounter in a practical application of this method to real data. In § 4.2-4 we describe how these difficulties can be overcome. In § 4.5 a method to infer the total mass within a circular aperture is described.

4.1. Kaiser and Squires algorithm—linear inversion Formula—

Since both κ and γ are linear combinations of the second derivatives of ψ , using the relation in Fourier space, one can obtain an expression for κ in terms of the complex shear γ ; that is, the relation (2·11) can be inverted.¹⁴⁾

To see this, we express the convergence $\kappa(\vec{\theta})$ by its Fourier transform $\hat{\kappa}(\vec{k})$ as

$$\kappa(\vec{\theta}) = \frac{1}{(2\pi)^2} \int d^2k \hat{\kappa}(\vec{k}) \exp(i\vec{k} \cdot \vec{\theta}). \quad (4.1)$$

In Fourier space, Eq. (2·11) reads

$$\hat{\gamma}(\vec{k}) = \frac{1}{\pi} \hat{\kappa}(\vec{k}) \hat{\mathcal{D}}(\vec{k}), \quad (4.2)$$

where $\hat{\kappa}(\vec{k})$ and $\hat{\mathcal{D}}(\vec{k})$ are the Fourier transforms of $\kappa(\vec{\theta})$ and $\mathcal{D}(\vec{\theta})$, respectively, and they are defined in the same way as in Eq. (4·1). The Fourier transform of the complex kernel $\mathcal{D}(\vec{\theta})$ defined by (2·12) is

$$\hat{\mathcal{D}}(\vec{k}) = \pi \frac{k_1^2 - k_2^2 + 2ik_1k_2}{|\vec{k}|^2}. \quad (4.3)$$

From Eq. (4·3), we find that $\hat{\mathcal{D}}\hat{\mathcal{D}}^* = \pi^2$, implying

$$\hat{\mathcal{D}}^{-1} = \pi^{-2} \hat{\mathcal{D}}^*. \quad (4.4)$$

Inserting Eq. (4·4) into Eq. (4·2) yields

$$\hat{\kappa}(\vec{k}) = \frac{1}{\pi} \hat{\gamma}(\vec{k}) \hat{\mathcal{D}}^*(\vec{k}). \quad (4.5)$$

This relation can be converted into the relation in the real $\vec{\theta}$ -space as follows:

$$\begin{aligned} \kappa(\vec{\theta}) - \kappa_0 &= \frac{1}{\pi} \int d^2\theta' \mathcal{D}^*(\vec{\theta} - \vec{\theta}') \gamma(\vec{\theta}') \\ &= \frac{1}{\pi} \int d^2\theta' \Re[\mathcal{D}^*(\vec{\theta} - \vec{\theta}') \gamma(\vec{\theta}')]. \end{aligned} \quad (4.6)$$

Here the constant κ_0 is inserted into the right-hand side of Eq. (4·6) because adding a uniform mass sheet does not change the shear (see Eq. (2·11)). In terms of the

tangential shear γ_t defined by Eq. (2·8), the inversion equation takes the following form:

$$\kappa(\vec{\theta}) - \kappa_0 = \frac{1}{\pi} \int d^2\theta' \frac{\gamma_t(\vec{\theta}'; \vec{\theta})}{|\vec{\theta} - \vec{\theta}'|^2}. \quad (4.7)$$

Thus we obtain an expression for the convergence $\kappa(\vec{\theta})$ in terms of the complex shear $\gamma(\vec{\theta})$ on the whole image plane.

To apply the *original* Kaiser and Squires algorithm to real data, the following assumptions must be made:

- (a) The cluster is linear in the sense that $\kappa \ll 1$ and $|\gamma| \ll 1$ everywhere.
- (b) Observational data are available over the entire space. This assumption may be dropped if the cluster is weak and small compared to the data field.
- (c) All background galaxies have the same *effective* redshift; i.e., all galaxies have approximately the same distance ratio $D_{\text{ds}}/D_{\text{s}}$.

If these assumptions hold, we can perform the direct mass reconstruction from the observed distortion field $\bar{\epsilon}(\vec{\theta})$. In the case of weak lensing, the shear γ is directly observable:

$$\gamma(\vec{\theta}) \approx \bar{\epsilon}(\vec{\theta}). \quad (4.8)$$

In practice, one has to replace the integral in Eq. (4.6) by a sum over a grid $\vec{\theta}_{ij}$ on which the shear is estimated. Using $\Sigma(\vec{\theta}) = \Sigma_{\text{cr}} \kappa(\vec{\theta})$, the surface-mass density $\Sigma(\vec{\theta})$ of the lensing cluster is given by

$$\Sigma(\vec{\theta}) - \Sigma_0 \approx \Sigma_{\text{cr}} \frac{1}{\pi} \int d^2\theta' \Re[\mathcal{D}^*(\vec{\theta} - \vec{\theta}') \bar{\epsilon}(\vec{\theta}')] \quad (4.9)$$

$$\approx \Sigma_{\text{cr}} \frac{a^2}{\pi} \sum_{i,j} \Re[\mathcal{D}^*(\vec{\theta} - \vec{\theta}_{ij}) \bar{\epsilon}(\vec{\theta}_{ij})], \quad (4.10)$$

where Σ_0 is a constant surface-mass density which comes from κ_0 in Eq. (4.6), and a is the separation of the grid points. In this way, we can reconstruct the cluster-mass distribution from the weak-shear field up to an additive constant Σ_0 .

The crucial result here is that the projected-mass distribution of a cluster can be determined only from the observed shear field, that is, only from information about the shapes of galaxy images. However, we must require rather strong assumptions in deriving Eq. (4.10). Here we enumerate several difficulties which we encounter in performing the cluster-mass reconstruction with the Kaiser and Squires algorithm.

(1) Application to non-linear clusters: Since the shear is observable only in the weak-lensing regime, the inversion algorithm described above cannot be applied to non-linear clusters.

(2) Finite size of the data field: The integral in the inversion formula extends over the entire two-dimensional space, while real data are available only in a finite region restricted by the CCD area. Because of the lack of information outside the data field, we are forced to set $\gamma = 0$ there, which is equivalent for circularly-symmetric clusters to vanishing total mass within the data field. This sharp cut-off of the integration leads to an unphysical negative mass density near the boundary. We thus suffer from artificial boundary effects in mass reconstructions owing to the sharp cut-off.

(3) Redshift distribution of source galaxies: Cluster-mass reconstructions depend on the assumed redshift of the background galaxies through the distance ratio $D_{\text{ds}}/D_{\text{s}}$ in Σ_{cr} . Since the redshifts of background galaxies are unknown, there is a scaling ambiguity in the obtained mass distribution. Moreover, if background galaxies are distributed in redshift, the assumption that the distance ratio $D_{\text{ds}}/D_{\text{s}}$ is the same for all background galaxies does not hold, especially for high-redshift clusters.

(4) Degeneracy of the solution for the cluster-mass inversion: We have seen that there exists a global transformation that leaves observable $\gamma(\vec{\theta})$ unchanged in the weak-lensing limit such that $\kappa(\vec{\theta}) \rightarrow \kappa(\vec{\theta}) + \kappa_0$, with an arbitrary constant κ_0 ; that is, the surface-mass density is determined only up to an additive constant from the observed shear field. We see in the next subsection that there exists a *general* global transformation that leaves the observable unchanged, which we encounter in all mass-reconstruction schemes based solely on image shapes.

4.2. Generalization of Kaiser and Squires algorithm for critical clusters

We have seen that the original Kaiser and Squires algorithm suffers from several difficulties. In this subsection we concentrate on the difficulties which we face in applying the Kaiser and Squires algorithm to non-linear clusters, where the shear γ is no longer a direct observable.

Seitz and Schneider¹⁷⁾ generalized the Kaiser and Squires algorithm to include critical clusters, i.e., clusters which can produce critical curves. This technique, to be discussed in this subsection, is based on Eq. (4.6), and we need the assumptions (b) and (c) discussed in the preceding subsection.

In order to extend the Kaiser and Squires method to the non-linear case, we express the inversion formula (4.6) with the reduced shear g . Using $\gamma = g(1 - \kappa)$ in Eq. (4.6), we have the integral equation

$$\kappa(\vec{\theta}) = \frac{1}{\pi} \int d^2\theta' \mathcal{D}^*(\vec{\theta} - \vec{\theta}') g(\vec{\theta}') [1 - \kappa(\vec{\theta}')]. \quad (4.11)$$

Here we have dropped a constant κ_0 in Eq. (4.11) because the shear γ is not an observable quantity in general. This equation can be formally expressed in an infinite power series as

$$\begin{aligned} \kappa(\vec{\theta}) &= \mathcal{G} - \mathcal{G} \circ \mathcal{G} + \mathcal{G} \circ \mathcal{G} \circ \mathcal{G} - \dots \\ &= \sum_{n=1}^{\infty} (-1)^{n-1} \mathcal{G}^n, \end{aligned} \quad (4.12)$$

where \mathcal{G} is the integral operator

$$\mathcal{G}(\vec{\theta}, \vec{\theta}') := \frac{1}{\pi} \int d^2\theta'' \mathcal{D}^*(\vec{\theta} - \vec{\theta}'') g(\vec{\theta}'') \times, \quad (4.13)$$

and $\mathcal{G}(\vec{\theta}, \vec{\theta}')$ acts on a function of $\vec{\theta}'$. The Kaiser and Squires method corresponds to the first-order approximation to this power series in the weak-lensing limit.

For non-critical clusters, i.e., $\det \mathcal{A}(\vec{\theta}) > 0$ for all $\vec{\theta}$, the reduced shear is directly observable: $g = \langle \epsilon \rangle_{\epsilon_s} \approx \bar{\epsilon}$. For critical clusters, however, the relation between ellipticity and lensing property depends on the parity of the image (see Eq. (3.9)), and

we cannot determine the parity locally. To take account of the parity distinction, we write the shear γ in the form

$$\begin{aligned}\gamma &= g(1 - \kappa) \\ &= H(1 - |g|)(1 - \kappa)\bar{\epsilon} + H(|g| - 1)(1 - \kappa)\frac{1}{\bar{\epsilon}^*}.\end{aligned}\quad (4.14)$$

Seitz and Schneider¹⁷⁾ proposed an iterative procedure to solve the non-linear inversion equation (4.11): From Eqs. (4.11) and (4.14), we have

$$\begin{aligned}&\kappa^{(n+1)}(\vec{\theta}) \\ &= \frac{1}{\pi} \int d^2\theta' H(1 - |g^{(n)}(\vec{\theta}')|) [1 - \kappa^{(n)}(\vec{\theta}')] \Re \left[\mathcal{D}^*(\vec{\theta} - \vec{\theta}') \bar{\epsilon}(\vec{\theta}') \right] \\ &+ \frac{1}{\pi} \int d^2\theta' H(|g^{(n)}(\vec{\theta}')| - 1) [1 - \kappa^{(n)}(\vec{\theta}')] \Re \left[\mathcal{D}^*(\vec{\theta} - \vec{\theta}') \frac{1}{\bar{\epsilon}^*(\vec{\theta}')} \right],\end{aligned}\quad (4.15)$$

where $g^{(n)} = \gamma^{(n)}/(1 - \kappa^{(n)})$ is the reduced shear in the n -th step of the iteration, and $\gamma^{(n)}$ is calculated by

$$\gamma^{(n)} = \frac{1}{\pi} \int d^2\theta' \mathcal{D}(\vec{\theta} - \vec{\theta}') \kappa^{(n)}(\vec{\theta}').\quad (4.16)$$

This iteration is performed by starting with $\kappa^{(0)}(\vec{\theta}) = \gamma^{(0)}(\vec{\theta}) = 0$ for all $\vec{\theta}$. Here we note that the first term on the right-hand side of Eq. (4.15) is the contribution to $\kappa(\vec{\theta})$ from the even-parity region, and the second term from the odd-parity region. In practice, of course, we use a discretized version of Eqs. (4.15) and (4.16).

In general, the observable quantity is not the shear γ but the reduced shear g (or $1/g^*$). We see that the reduced shear g is invariant under the transformation

$$\kappa(\vec{\theta}) \rightarrow \lambda\kappa(\vec{\theta}) + (1 - \lambda), \quad \gamma(\vec{\theta}) \rightarrow \lambda\gamma(\vec{\theta})\quad (4.17)$$

with an arbitrary scalar constant $\lambda \neq 0$;¹⁶⁾ this transformation is equivalent to scaling the Jacobian matrix $\mathcal{A}(\vec{\theta})$ with λ :

$$\mathcal{A}(\vec{\theta}) \rightarrow \lambda\mathcal{A}(\vec{\theta}) = \lambda \begin{pmatrix} 1 - \kappa - \gamma_1 & -\gamma_2 \\ -\gamma_2 & 1 - \kappa + \gamma_1 \end{pmatrix}.\quad (4.18)$$

Thus we can determine $\kappa(\vec{\theta})$ only up to a constant. This is because we use the information only regarding the image shapes. We see that this transformation leaves the critical curves $\det\mathcal{A}(\vec{\theta}) = 0$ invariant. This indicates that we cannot determine the constant λ even if GLAs, which are tracers of critical curves, are observed. Further, the curve $\kappa(\vec{\theta}) = 1$, on which the gravitational distortions disappear, is left invariant under the transformation (4.17). We can, however, constrain the value of λ by requiring that the surface-mass density is positive everywhere, which yields a lower bound on $\kappa(\vec{\theta})$.

A possible method to break this degeneracy is to employ the information about magnification effects. That is, we employ the fact that the magnification μ transforms as

$$\mu(\vec{\theta}) \rightarrow \lambda^{-2}\mu(\vec{\theta})\quad (4.19)$$

under the transformation (4-17). Since gravitational magnification changes the size of a galaxy image and the number density of background galaxies, we can in principle break the mass degeneracy by combining the shear analysis with such magnification effects.³²⁾⁻³⁴⁾

4.3. Finite field inversion of the cluster mass distribution

Both the inversion methods described above are based on Eq. (4-6) which involves the convolution integral of the shear over the entire two-dimensional space. If one tries to apply the inversion formula (4-6) to real data which are limited by the finite size of the CCD frame, then artificial boundary effects cannot be avoided.

In this subsection we review the finite-field inversion method for the cluster-mass distribution derived by Seitz and Schneider.²⁰⁾ This inversion method has been introduced to optimize the observational data, that is, to minimize the statistical errors due to noise. We assume, for simplicity, that all background galaxies have about the same distance ratio $D_{\text{ds}}/D_{\text{s}}$ as in § 4.1 and 4.2. We shall discuss the redshift distribution of background galaxies in § 4.4.

All finite-field methods start from the fact that the gradient of the convergence κ is related to the first derivatives of the shear γ :¹⁵⁾

$$\vec{\nabla}_{\theta}\kappa(\vec{\theta}) = \begin{pmatrix} \gamma_{1,1} + \gamma_{2,2} \\ \gamma_{2,1} - \gamma_{1,2} \end{pmatrix} \equiv \vec{U}(\vec{\theta}). \quad (4-20)$$

In the weak-lensing limit where the shear γ is a direct observable, we can obtain the vector field $\vec{U}(\vec{\theta})$ from the observed distortion field. However, the shear γ is not an observable in general. Inserting $\gamma = g(1 - \kappa)$ into Eq. (4-20), we obtain the relation¹⁵⁾

$$\vec{\nabla}_{\theta}K(\vec{\theta}) = \frac{-1}{1 - |g|^2} \begin{pmatrix} 1 - g_1 & -g_2 \\ -g_2 & 1 + g_1 \end{pmatrix} \begin{pmatrix} g_{1,1} + g_{2,2} \\ g_{2,1} - g_{1,2} \end{pmatrix} \equiv u(\vec{\theta}), \quad (4-21)$$

where $K(\vec{\theta})$ is the scalar field defined by

$$K(\vec{\theta}) := \ln[1 - \kappa(\vec{\theta})]. \quad (4-22)$$

For a non-critical cluster, we can construct the vector field $\vec{u}(\vec{\theta})$ in terms of the observable quantity $g(\vec{\theta}) = \langle \epsilon \rangle_{\epsilon_s}(\vec{\theta}) \approx \bar{\epsilon}(\vec{\theta})$. Hence, the relation (4-21) can be used to reconstruct the surface-mass density from the shear field on a finite region \mathcal{U} . Since $\vec{u}(\vec{\theta})$ in Eq. (4-21) is a gradient field, the differential equations (4-21) can be solved up to an additive constant by integrating $\vec{u}(\vec{\theta})$ from an arbitrary point $\vec{\theta}_0$ to the point $\vec{\theta}$ along an arbitrary smooth curve \vec{l} :

$$K(\vec{\theta}) = K(\vec{\theta}_0) + \int_{\vec{\theta}_0}^{\vec{\theta}} d\vec{l} \cdot \vec{u}(\vec{l}). \quad (4-23)$$

However, the vector field $\vec{u}(\vec{\theta})$ is obtained from noisy data, so that it will contain a rotational component. Therefore, $\vec{u}(\vec{\theta})$ is not a gradient field in general; in other

words, mass reconstructions from line integrals of Eq. (4·20) or (4·21) depend on the choice of the integration path.

Seitz and Schneider²⁰⁾ have explicitly taken into account the noise component of the vector field $\vec{u}(\vec{\theta})$ obtained from the observed distortion field by decomposing $\vec{u}(\vec{\theta})$ into gradient and rotational components:

$$\vec{u}(\vec{\theta}) = \vec{\nabla}_{\theta} K(\vec{\theta}) + \vec{\nabla}_{\theta} \times s(\vec{\theta}), \quad (4·24)$$

where

$$\vec{\nabla}_{\theta} \times s(\vec{\theta}) := \begin{pmatrix} \partial s / \partial \theta_2 \\ -\partial s / \partial \theta_1 \end{pmatrix}. \quad (4·25)$$

Here $s(\vec{\theta})$ is a scalar field which is assumed to account for the noise part within the data field \mathcal{U} . The decomposition (4·24) can be determined uniquely by requiring that the average of $\vec{\nabla}_{\theta} \times s(\vec{\theta})$ within \mathcal{U} vanishes, which is reasonable if the rotational component $\vec{\nabla}_{\theta} \times s(\vec{\theta})$ is due to noise. This requirement can be satisfied if $s(\vec{\theta})$ satisfies the condition

$$s(\vec{\theta}) = \text{const on the boundary } \partial\mathcal{U} \text{ of } \mathcal{U}. \quad (4·26)$$

(This is not a necessary but a sufficient condition.) If the condition (4·26) is satisfied, the scalar field $K(\vec{\theta})$ can be obtained from the vector field (4·24):

$$K(\vec{\theta}) - \bar{K} = \int_{\mathcal{U}} d^2\theta' \vec{H}(\vec{\theta}', \vec{\theta}) \cdot \vec{u}(\vec{\theta}') \quad (4·27)$$

with

$$\vec{H}(\vec{\theta}', \vec{\theta}) := -\vec{\nabla}_{\theta'} \mathcal{L}(\vec{\theta}', \vec{\theta}). \quad (4·28)$$

Here \bar{K} is a constant which represents the average of $K(\vec{\theta})$ within the data field \mathcal{U} , and $\mathcal{L}(\vec{\theta}', \vec{\theta})$ is the solution of the Neumann boundary problem

$$\Delta_{\theta'} \mathcal{L}(\vec{\theta}', \vec{\theta}) = \delta^2(\vec{\theta} - \vec{\theta}') - \frac{1}{A} \quad \forall \vec{\theta}' \in \mathcal{U} \quad (4·29)$$

$$\vec{n}(\vec{\theta}') \cdot \vec{\nabla}_{\theta'} \mathcal{L}(\vec{\theta}', \vec{\theta}) = 0 \quad \forall \vec{\theta}' \in \partial\mathcal{U}, \quad (4·30)$$

where A is the area of the data field \mathcal{U} , and \vec{n} is the unit vector orthogonal to the boundary $\partial\mathcal{U}$; $\mathcal{L}(\vec{\theta}', \vec{\theta})$ is solved uniquely up to an additive constant, so that the kernel $\vec{H}(\vec{\theta}', \vec{\theta})$ is determined uniquely for a given boundary $\partial\mathcal{U}$. The solution for two special geometries, a circle and a rectangle, is derived in Ref. 20). The kernel $\vec{H}(\vec{\theta}', \vec{\theta})$ is called *noise filtering* because it filters out the rotational noise component. We note that we can replace (K, \vec{u}) in Eq. (4·27) with (κ, \vec{U}) , because κ and \vec{U} are related to each other through the same relation ($\vec{\nabla}_{\theta} \kappa = \vec{U}$) as that relating K and \vec{u} ($\vec{\nabla}_{\theta} K = \vec{u}$); that is,

$$\kappa(\vec{\theta}) - \bar{\kappa} = \int_{\mathcal{U}} d^2\theta' \vec{H}(\vec{\theta}', \vec{\theta}) \cdot \vec{U}(\vec{\theta}'), \quad (4·31)$$

where $\bar{\kappa}$ is the average of $\kappa(\vec{\theta})$ within the data field \mathcal{U} . We see from Eqs. (4·27) and (4·23) that $K(\vec{\theta}) = \ln[1 - \kappa(\vec{\theta})]$ can be obtained up to an additive constant \bar{K} ; i.e., $\kappa(\vec{\theta})$ is determined only up to the global transformation

$$\kappa(\vec{\theta}) \rightarrow \lambda \kappa(\vec{\theta}) + (1 - \lambda) \quad (4·32)$$

with an arbitrary constant $\lambda \neq 0$.

Several authors have developed inversion techniques +that require data only on a finite field.^{15), 18) - 21)} Seitz and Schneider²⁰⁾ have shown that there exist an infinite number of finite-field formulae, which are mathematically equivalent but different in their dependence on the noise due to the discreteness of data or the intrinsic ellipticity of the background galaxies. They also analyzed quantitatively the power spectra of the error fields for the mass maps reconstructed with synthetic data using different inversion methods: the non-linear version of the Kaiser and Squires inversion equation (4.15), the finite-field inversion equation with the noise-filtering kernel and two other finite-field inversion equations. The main results obtained there are (i) the inversion formula (4.27) performs better than the other two finite-field formulae, (ii) the noise for the finite-inversion (4.27) is more uniform than that for the other inversions over the data field and (iii) concerning the small-scale error, the modified Kaiser and Squires inversion (4.15) works best of all the inversion tested there, while it suffers from artificial boundary effects. They concluded from their results that the finite-field inversion with the noise-filtering kernel is the most accurate of all the inversion formulae used in their analysis. Lombardi and Bertin³⁵⁾ have obtained expressions for the errors on the mass maps reconstructed with various inversion formulae and shown that a rotation-free kernel, such as the noise-filtering kernel, should be used in order to optimize the reconstruction procedure. The analytical results obtained by Lombardi and Bertin confirm the conclusion of Seitz and Schneider.²⁰⁾

4.4. The General cluster mass reconstruction algorithm

Up to this point we have only dealt with the case where all background galaxies have the same effective redshift, i.e., all background galaxies have about the same distance ratio $D_{\text{ds}}/D_{\text{s}}$. This approximation is fairly good if the cluster redshift is relatively low and almost all galaxies have high redshifts. For high-redshift clusters, however, the redshift distribution of the source galaxies has to be taken into account in the inversion procedure explicitly. We review in this subsection the mass-reconstruction scheme developed by Seitz and Schneider,³²⁾ which includes the case where background galaxies are distributed in redshift. Here we fix the lens redshift z_{d} and express lensing properties explicitly as functions of the source redshift z (e.g., $\kappa(\vec{\theta}) \equiv \kappa(\vec{\theta}, z)$).

If we define the *relative lensing strength* $w(z)$ for a source with redshift z by

$$w(z) := H(z - z_{\text{d}}) \frac{\Sigma_{\text{cr}, \infty}}{\Sigma_{\text{cr}}(z)} \quad (4.33)$$

with

$$\Sigma_{\text{cr}, \infty} := \lim_{z \rightarrow \infty} \Sigma_{\text{cr}}(z), \quad (4.34)$$

then the convergence and the shear for a source at redshift z can be expressed as

$$\kappa(\vec{\theta}, z) = H(z - z_{\text{d}}) \frac{\Sigma(\vec{\theta})}{\Sigma_{\text{cr}}(z)} = w(z) \frac{\Sigma(\vec{\theta})}{\Sigma_{\text{cr}, \infty}} \equiv w(z) \kappa_{\infty}(\vec{\theta}) \quad (4.35)$$

and

$$\gamma(\vec{\theta}, z) \equiv w(z) \gamma_\infty(\vec{\theta}), \quad (4.36)$$

respectively. Note that $\kappa(\vec{\theta}, z) = \gamma(\vec{\theta}, z) = 0$ for a source with redshift $z \leq z_d$. The function $w(z)$ can be calculated for a given background cosmology; for an Einstein-de Sitter universe ($\Omega_0 = 1$), $w(z)$ is given by

$$w(z) = H(z - z_d) \frac{\sqrt{1+z} - \sqrt{1+z_d}}{\sqrt{1+z} - 1}, \quad (4.37)$$

and $\Sigma_{\text{cr},\infty}$ is calculated to be

$$\begin{aligned} \Sigma_{\text{cr},\infty} &= \frac{cH_0}{8\pi G} \frac{(1+z_d)^2}{\sqrt{1+z_d} - 1} \\ &= 1.39 \times 10^{14} \frac{(1+z_d)^2}{\sqrt{1+z_d} - 1} h_{50} M_\odot \text{Mpc}^{-2}. \end{aligned} \quad (4.38)$$

From Eqs. (2.17), (4.35) and (4.36), the magnification $\mu(\vec{\theta}, z)$ of an image at angular position $\vec{\theta}$ and redshift z is given by

$$\begin{aligned} \mu(\vec{\theta}, z) &= \frac{1}{|\det \mathcal{A}(\vec{\theta}, z)|} \\ &= \frac{1}{\left| [1 - w(z) \kappa_\infty(\vec{\theta})]^2 - w^2(z) |\gamma_\infty(\vec{\theta})|^2 \right|}. \end{aligned} \quad (4.39)$$

If $\det \mathcal{A}(\vec{\theta}, \infty) = [1 - \kappa_\infty(\vec{\theta})]^2 - |\gamma_\infty(\vec{\theta})|^2 > 0$ for all $\vec{\theta}$, then the cluster is non-critical for all source redshifts.

As we have seen in § 3, only g or $1/g^*$ is accessible to the observable quantity ϵ . For a fixed source redshift z , the expectation value of $\epsilon^n(\vec{\theta})$ is

$$\langle \epsilon^n \rangle_{\epsilon_s}(\vec{\theta}, z) = \begin{cases} g^n(\vec{\theta}, z) & \text{for } |g(\vec{\theta}, z)| \leq 1, \\ 1/g^{*n}(\vec{\theta}, z) & \text{for } |g(\vec{\theta}, z)| > 1 \end{cases} \quad (4.40)$$

(see Eq. (3.13)), where

$$g(\vec{\theta}, z) = \frac{\gamma(\vec{\theta}, z)}{1 - \kappa(\vec{\theta}, z)} = \frac{w(z) \gamma_\infty(\vec{\theta})}{1 - w(z) \kappa_\infty(\vec{\theta})}. \quad (4.41)$$

We then consider the case where source galaxies are distributed in redshift. Let $p_z(z) dz$ be the probability that the source redshift is within dz around z ; this is a simple approximation, because the gravitational magnification changes the observed number density of galaxies, so that the probability distribution of the observed source redshift depends on the magnification $\mu(\vec{\theta}, z)$.³³⁾ This simplification is justified if the overall magnification is found to be small, or if the dependence of the galaxy redshift distribution on the flux is weak.

If $p_z(z)$ is assumed to be known, the expectation value of ϵ^n can be expressed by

$$\begin{aligned}
\langle \epsilon^n \rangle_{\epsilon_s, z} &:= \int_0^\infty dz p_z(z) \int d^2 \epsilon_s p_{\epsilon_s} \epsilon^n(\epsilon_s, g(z)) \\
&= \int_{\det A(z) \geq 0} dz p_z(z) g^n(z) + \int_{\det A(z) < 0} dz p_z(z) \left(\frac{1}{g^*(z)} \right)^n \\
&= \gamma_\infty^n \int_{\det A(w) \geq 0} dw p_w(w) \left(\frac{w}{1 - \kappa_\infty w} \right)^n \\
&\quad + \frac{\gamma_\infty^n}{|\gamma_\infty|^{2n}} \int_{\det A(w) < 0} dw p_w(w) \left(\frac{1 - \kappa_\infty w}{w} \right)^n \\
&\equiv \gamma_\infty^n \left[X_n(\kappa_\infty, \gamma_\infty) + \frac{1}{|\gamma_\infty|^{2n}} Y_n(\kappa_\infty, \gamma_\infty) \right], \tag{4.42}
\end{aligned}$$

where $p_w(w)$ is the probability distribution function of w , which is given by $p_w(w) dw = p_z dz$. Here the functions X_n and Y_n depend on κ_∞ and γ_∞ by

$$\begin{aligned}
X_n(\kappa_\infty, \gamma_\infty) &= \left(\int_0^{\min(1, 1/(\kappa_\infty + |\gamma_\infty|))} + \int_{\frac{1}{\max(1, \kappa_\infty - |\gamma_\infty|)}}^1 \right) \\
&\quad \times dw p_w(w) \left(\frac{w}{1 - \kappa_\infty w} \right)^n, \tag{4.43}
\end{aligned}$$

$$Y_n(\kappa_\infty, \gamma_\infty) = \int_{\min(1, 1/(\kappa_\infty + |\gamma_\infty|))}^{\frac{1}{\max(1, \kappa_\infty - |\gamma_\infty|)}} dw p_w(w) \left(\frac{1 - \kappa_\infty w}{w} \right)^n. \tag{4.44}$$

Now we have the local relation between the expectation value of ϵ and the lensing properties,

$$\gamma_\infty(\vec{\theta}) = \langle \epsilon \rangle_{\epsilon_s, z}(\vec{\theta}) \left[X_1(\kappa_\infty(\vec{\theta}), \gamma_\infty(\vec{\theta})) + \frac{1}{|\gamma_\infty(\vec{\theta})|^2} Y_1(\kappa_\infty(\vec{\theta}), \gamma_\infty(\vec{\theta})) \right]^{-1}. \tag{4.45}$$

In a practical application, the redshift-averaged ellipticity $\langle \epsilon \rangle_{\epsilon_s, z}(\vec{\theta})$ must be replaced by the observed ellipticity $\bar{\epsilon}(\vec{\theta})$ defined by Eq. (3.15). In the weak-lensing limit (i.e., $\kappa_\infty \ll 1$ and $|\gamma_\infty| \ll 1$), we have

$$X_n(\kappa_\infty, \gamma_\infty) \approx \langle w^n \rangle; \quad Y_n(\kappa_\infty, \gamma_\infty) = 0 \tag{4.46}$$

with

$$\langle w^n \rangle := \int_0^1 dw p_w(w) w^n, \tag{4.47}$$

and therefore the shear γ_∞ is observable:

$$\gamma_\infty(\vec{\theta}) \approx \bar{\epsilon}(\vec{\theta}) / \langle w \rangle. \tag{4.48}$$

That is, in the weak-lensing limit, the situation is the same as in the case where all sources have the same redshift z such that $w(z) = \langle w \rangle$.

In *general* cluster-mass reconstructions, the finite-field inversion formula (4.31) can be used:³²⁾

$$\kappa_\infty(\vec{\theta}) - \bar{\kappa}_\infty = \int_{\mathcal{U}} d^2\theta' \vec{H}(\vec{\theta}', \vec{\theta}) \cdot \vec{U}_\infty(\vec{\theta}') \quad (4.49)$$

with

$$\vec{U}_\infty(\vec{\theta}) := \begin{pmatrix} (\gamma_\infty)_{1,1} + (\gamma_\infty)_{2,2} \\ (\gamma_\infty)_{2,1} - (\gamma_\infty)_{1,2} \end{pmatrix}. \quad (4.50)$$

Here $\bar{\kappa}_\infty$ is the (unknown) average of $\kappa_\infty(\vec{\theta})$ within the data field \mathcal{U} . Inserting Eq. (4.45) in Eq. (4.49), we have the integral equation for $\kappa_\infty(\vec{\theta})$, which can be solved iteratively. Starting the iteration with $\kappa_\infty^{(0)}(\vec{\theta}) = \gamma_\infty^{(0)}(\vec{\theta}) = 0$ for all $\vec{\theta}$, we calculate $\kappa_\infty^{(n)}$ and $\gamma_\infty^{(n)}$ for $n \geq 1$ by

$$\kappa_\infty^{(n+1)}(\vec{\theta}) - \bar{\kappa}_\infty = \int_{\mathcal{U}} d^2\theta' \vec{H}(\vec{\theta}', \vec{\theta}) \cdot \vec{U}_\infty^{(n+1)}(\vec{\theta}'), \quad (4.51)$$

$$\gamma_\infty^{(n+1)} = \bar{\epsilon} \left[X_1(\kappa_\infty^{(n)}, \gamma_\infty^{(n)}) + \frac{1}{|\gamma_\infty^{(n)}|^2} Y_1(\kappa_\infty^{(n)}, \gamma_\infty^{(n)}) \right]^{-1}. \quad (4.52)$$

Here the vector field $\vec{U}_\infty^{(n+1)}(\vec{\theta})$ is calculated from Eq. (4.50) with $\gamma_\infty^{(n+1)}(\vec{\theta})$.

It can be seen from Eq. (4.51) that this iterative procedure still contains the undetermined constant $\bar{\kappa}_\infty$. Hence, this inversion algorithm involves a global transformation that leaves the observable invariant. In addition, the dependence of the resulting mass distribution on the constant $\bar{\kappa}_\infty$ is highly non-linear, so that this transformation cannot be determined analytically. In the case of weak lensing ($\kappa_\infty \ll 1$ and $\gamma_\infty \ll 1$), we have seen that the mass reconstruction depends only on $\langle w \rangle$, so that the global invariance transformation is equivalent to adding a constant. If the cluster is non-critical for all sources (i.e., $\det \mathcal{A}(\infty, \vec{\theta}) > 0$ for all $\vec{\theta}$), then Y_n vanishes and X_n depends only on κ_∞ , yielding a somewhat simple relation:

$$\langle \epsilon^n \rangle_{\epsilon_s, z} = \gamma_\infty^n X_n(\kappa_\infty). \quad (4.53)$$

On the other hand, an approximation for the function $X_1(\kappa_\infty)$ is

$$X_1(\kappa_\infty) \approx \frac{\langle w \rangle}{1 - \kappa_\infty \frac{\langle w^2 \rangle}{\langle w \rangle}}, \quad (4.54)$$

which is quite accurate for non-linear but not very strong clusters.³²⁾ In this case, the global invariance transformation becomes

$$\kappa_\infty(\vec{\theta}) \rightarrow \lambda \kappa_\infty(\vec{\theta}) + \frac{(1 - \lambda) \langle w \rangle}{\langle w^2 \rangle} \quad (4.55)$$

with an arbitrary constant $\lambda \neq 0$.

4.5. Cluster mass estimates from shear fields

In the previous subsections we have described the cluster-mass reconstruction methods based on the shear analysis. One of the goals of such studies is to obtain the total mass of a cluster within a given region. In estimating the cluster mass inside a given aperture, one method to obtain the aperture mass is to use the reconstructed two-dimensional mass distribution. However, the resulting mass map from the shear field will be noisy because of the discreteness of the galaxy images, intrinsic source ellipticities, etc. In addition, it is difficult to estimate an error for the local convergence since the errors of the reconstructed convergence at different points will be strongly correlated. In this subsection we describe a method to infer the projected cluster mass inside circular apertures from weak lensing without reconstructing the entire mass distribution.

First, we define a polar coordinate system (ϑ, φ) centered on a point $\vec{\theta}_0$ such that

$$\vec{\theta}(\vartheta, \varphi) = \begin{pmatrix} \vartheta \cos \varphi \\ \vartheta \sin \varphi \end{pmatrix} + \vec{\theta}_0. \quad (4.56)$$

Then the convergence averaged within a circle of radius ϑ around $\vec{\theta}_0$ is given by

$$\bar{\kappa}(\vartheta) := \frac{1}{\pi\vartheta^2} \int_0^\vartheta d\vartheta' \vartheta' \oint d\varphi' \kappa(\vec{\theta}(\vartheta', \varphi')). \quad (4.57)$$

Using the two-dimensional version of Gauss's theorem, this quantity can be transformed into

$$\bar{\kappa}(\vartheta) = \langle \kappa \rangle(\vartheta) + \langle \gamma_t \rangle(\vartheta; \vec{\theta}_0), \quad (4.58)$$

where the angular brackets denote the average over a circle of radius ϑ , e.g.,

$$\langle \gamma_t \rangle(\vartheta; \vec{\theta}_0) := \oint \frac{d\varphi}{2\pi} \gamma_t(\vec{\theta}(\vartheta, \varphi); \vec{\theta}_0) \quad (4.59)$$

with the tangential shear $\gamma_t(\vec{\theta}; \vec{\theta}_0)$ relative to the origin $\vec{\theta}_0$ of the coordinate system.

On the other hand, $\bar{\kappa}(\vartheta)$ can be expressed as

$$\bar{\kappa}(\vartheta) = \frac{2}{\vartheta^2} \int_0^\vartheta d\vartheta' \vartheta' \langle \kappa \rangle(\vartheta'). \quad (4.60)$$

From Eqs. (4.58) and (4.60), we have

$$\frac{d\bar{\kappa}(\vartheta)}{d \ln \vartheta} = -2 \langle \gamma_t \rangle(\vartheta; \vec{\theta}_0). \quad (4.61)$$

Integrating Eq. (4.61) between radii ϑ and ϑ' ($> \vartheta$), we obtain the so-called ζ -statistic,²²⁾

$$\zeta(\vartheta, \vartheta') := \bar{\kappa}(\vartheta) - \bar{\kappa}(\vartheta, \vartheta') = \frac{2\vartheta'^2}{\vartheta'^2 - \vartheta^2} \int_\vartheta^{\vartheta'} \frac{d\vartheta''}{\vartheta''} \langle \gamma_t \rangle(\vartheta''; \vec{\theta}_0), \quad (4.62)$$

where $\bar{\kappa}(\vartheta, \vartheta')$ is the average of the convergence within an annulus between ϑ and ϑ' :

$$\bar{\kappa}(\vartheta, \vartheta') := \frac{1}{\pi(\vartheta'^2 - \vartheta^2)} \int_\vartheta^{\vartheta'} d\vartheta'' \vartheta'' \langle \kappa \rangle(\vartheta''). \quad (4.63)$$

In the weak-lensing limit (i.e., $\kappa \ll 1$ and $|\gamma| \ll 1$), the ζ -statistic can be determined uniquely from the shear field, because the invariance transformation, which corresponds to an additive constant to κ , cancels out on the right-hand side of Eq. (4.62).

Since $\bar{\kappa}(\vartheta, \vartheta')$ has a non-negative value, $\zeta(\theta, \theta')$ yields a lower limit on $\bar{\kappa}(\vartheta)$; that is, the quantity $\pi(D_d\vartheta)^2 \Sigma_{\text{cr}} \zeta(\vartheta, \vartheta')$ yields a lower limit on the lensing mass inside a circular aperture of radius ϑ . Thus we can infer the lensing mass inside a circular boundary from the data outside the boundary in the weak-lensing limit. The ζ -statistic is useful in estimating the total cluster mass within the data field.

We note that the shape of an aperture need not be restricted to a circle. Aperture masses for arbitrary aperture shapes are dealt with in Ref. 36).

§5. Observational Studies of Weak Lensing

This section reviews the observational studies of galaxy clusters based on the weak-lensing analysis. In § 5.1 we summarize some observational results from weak lensing. In § 5.2 we discuss the prospects of weak-lensing analysis on clusters with the upcoming 8.3 m *Subaru* telescope.

5.1. Observational results

The non-parametric methods for cluster-mass reconstructions by means of weak lensing have been widely used in investigating cluster properties in recent years. The pioneering work in this field was carried out by Kaiser and Squires,¹⁴⁾ who derived an exact inversion equation for the two-dimensional mass density of the deflector in terms of the tidal component of the gravitational field, namely the shear which is observable in the weak-lensing regime. The direct mass-reconstruction method of Kaiser and Squires and its variants were then applied to real clusters. In practice, these mass-reconstruction methods were mainly used to obtain the morphology of the mass distribution in a cluster. On the other hand, the ζ -statistic was often used in the cluster-mass estimations, as mentioned in § 4.5. We summarize in Table I some results of the weak-lensing analysis on clusters.

Fahlman et al.²²⁾ first applied the Kaiser and Squires method to the X-ray luminous cluster MS 1224+20 at redshift 0.33. The shear field for this cluster was measured from the observational data obtained with the 3.6 m *Canada-France-Hawaii Telescope* (CFHT), and the two-dimensional mass map was derived from the shear field. The location of the main peak of the resulting mass map is in good agreement with that of the optical and X-ray centroid. The mass estimates were performed using the ζ -statistic (4.62) within a circular aperture of radius 2'.76 (corresponding to a physical radius of $0.96 h_{50}^{-1}$ Mpc for an Einstein-de Sitter universe) centered on the mass peak. They obtained a lower bound on the aperture mass interior to radius $0.96 h_{50}^{-1}$ Mpc to be $\simeq 7.0 \times 10^{14} h_{50}^{-1} M_{\odot}$, which corresponds to a mass-to-light ratio of $M/L \sim 400 h_{50}$ in solar units. The mass estimate for this cluster from weak-lensing analysis is about three times larger than that from virial analysis.

Smail et al.³⁷⁾ analyzed three clusters which span a wide redshift range, $z_d \in [0.26, 0.89]$. Two of these clusters (Cl 1455+22, $z_d = 0.26$; Cl 0016+16, $z_d = 0.55$)

were selected for their high X-ray luminosities, and the other (Cl 1603+43, $z_d = 0.89$) was optically discovered and has a low X-ray luminosity. They detected clear lensing signals in the two lower-redshift clusters, while no significant lensing signal was detected in the highest-redshift cluster Cl 1603+43. They concluded from their results that the absence of any lensing signal for their highest-redshift cluster is ascribed to the absence of a high-redshift population of background galaxies with $I < 25$. On the other hand, Luppino and Kaiser²⁴⁾ argued that the failure of Smail et al. to detect weak lensing in Cl 1603+43 is simply due to the fact that this cluster is not massive enough to produce a detectable shear signal. The detection of significant shear signals in high-redshift clusters (MS 1054-03, $z_d = 0.83$;²⁴⁾ MS 1137+66, $z_d = 0.783$;³⁸⁾ RXJ 1716+67, $z_d = 0.813$ ³⁸⁾) indicates that the great part of background galaxies are at redshifts of the order of unity, supporting the argument by Luppino and Kaiser.

Seitz et al.²⁵⁾ applied a direct mass-reconstruction method to the distant cluster Cl 0939+47 at redshift $z_d = 0.41$, observed with the *Wide Field Planetary Camera 2* (WFPC2) on the *Hubble Space Telescope* (HST). Owing to the high redshift of this cluster and the small field-of-view of the WFPC2, the mass-reconstruction scheme described in § 4.4—which takes into account the redshift distribution of the background galaxies and is based on the finite-field inversion equation—was used. Assuming a particular form of the parameterized distribution function of the source redshift, they reconstructed two-dimensional mass maps for several sets of the parameters. They found a strong correlation between the reconstructed mass map and the light distribution of the bright cluster galaxies. The main mass and light maximum agree well with a maximum in the X-ray image from the *ROSAT*/PSPC observation.³⁹⁾ They also found a magnification effect on the observed number density of background galaxies, by which they removed the mass degeneracy.

Direct mass-reconstruction methods have also been applied to the QSO fields. From the CFHT observation, Fisher et al.⁴⁰⁾ measured a weak gravitational shear induced by the cluster at a redshift of 0.355 in the field of the double QSO 0957+561, which is a multiply-lensed system with a well-studied time delay. They reconstructed a two-dimensional mass map in this field from the measured shear field in order to construct a detailed model for the lens system which consists of a primary lensing galaxy and the cluster containing this galaxy. The resulting mass distribution is consistent with a spherical cluster possessing a mass peak slightly offset from the position of the primary lensing galaxy. The obtained projected mass within a circular aperture of radius $1 h_{50}^{-1}$ Mpc centered on the mass peak is $3.9 \pm 1.2 \times 10^{14} h_{50}^{-1} M_{\odot}$.

Several authors have compared cluster-mass estimates from weak lensing and those from other methods. Detailed quantitative comparisons of cluster-mass estimates on scales ~ 1 Mpc show that mass estimates from weak-lensing analysis are consistent with those from X-ray analysis based on the hydrostatic equilibrium of the ICM with the gravitational potential (Abell 2218;⁴¹⁾ Abell 2390;⁴²⁾ Abell 2163^{43), 44)}).

5.2. Observation with the Subaru telescope

The weak-lensing analysis of galaxy clusters requires quite a large number density ($\sim 50 \text{ arcmin}^{-2}$) of galaxy images with sufficient detail and accuracy in order to obtain a reliable shear measurement. Hence, cluster-mass reconstructions based on the weak-shear field rely on the power of telescopes and instruments to be used. Moreover, for ground-based observations, the effect of atmospheric seeing—the circularization of galaxy images—will reduce the lensing strength considerably since most of the background galaxies are quite small and faint. Hence, an excellent seeing condition (sub-arcsec) as well as a high angular resolution is required for the ground-based weak-lensing analysis.

On the other hand, the space-based deep *HST*/WFPC2 observation provides us with a large galaxy-number density without the seeing effect. Hence, it is a natural consequence that *HST*/WFPC2 observations have been frequently used in weak-lensing analysis in recent years.^{25), 45), 46)} However, in contrast to these advantages, the *HST*/WFPC2 observations have a fatal weakness from the theoretical point of view. As mentioned above, a mass reconstruction based only on the shear field suffers from mass degeneracy. If the cluster-mass distribution extends beyond the observed data field, we cannot uniquely determine the solution for the cluster-mass inversion from the shear field. In this case, we obtain only a lower limit on the cluster mass in the observed field. Moreover, since the dependence of mass reconstructions on the free parameter $\bar{\kappa}_\infty$ (see § 4.3) is highly non-linear for a high-redshift and super-critical cluster, even the resulting morphology of the cluster could be uncertain, depending on the choice of the parameter. In addition, the irregular shape of the WFPC2 frame will also make a mass reconstruction difficult to realize. Hence, both the requirements of a *large galaxy-number density* and a *wide field-of-view* are needed for a reliable mass reconstruction.

The *Subaru telescope* is among such telescopes which ideally satisfy both the requirements. Subaru is the Japanese 8.3 m optical-infrared ground-based telescope at the summit of Mauna Kea, Hawaii. Among the observational instruments for Subaru, Suprime-Cam (Subaru Prime Focus Camera) is the most suitable for weak-lensing analysis. Suprime-Cam at the F/2.3 prime focus has a wide-field imaging, covering a $30' \times 24'$ field-of-view with a $0.''2/\text{pixel}$ resolution.⁴⁷⁾ This corresponds to a physical scale of about $7.6 \times 6.1h_{50}^{-2} \text{ Mpc}^2$ at a moderate redshift of 0.2 for an Einstein-De Sitter universe. Weak-lensing analysis using the Subaru telescope with Suprime-Cam can probe the mass distribution on large scales ($\sim 10 \text{ Mpc}$) where the formation of gravitational structures is still in progress. Such studies can provide unique, invaluable information on the distribution of dark matter and Ω_0 . For example, the super cluster MS0302+17 containing three clusters (Cl 0303+1706, $z_d = 0.418$; MS 0302+1659, $z_d = 0.426$; MS 0302+1717, $z_d = 0.425$) is of interest to investigate such problems.⁴⁸⁾

Table I. Summary of observational studies of clusters from weak lensing.

Cluster	$z_d^a)$	$r^b)$ (h_{50}^{-1})	$M(< r)^c)$ (h_{50}^{-1})	$M/L^d)$ (h_{50})	Telescope $e)$	Ref. $f)$
Abell 1689	0.184	3	89	200±30	CTIO $i)$	49), 51)
Abell 2163	0.208	0.90	13±7	150± 50	CFHT $ii)$	43), 51)
Abell 2218	0.175	0.8	7.8±1.4	220± 40	CFHT	41)
		0.4	2.10±0.38	155	<i>HST</i> $iii)$	45)
Abell 2390	0.231	1.15	19.5±6.5	160±45	CFHT	42), 51)
AC 118 (=Abell 2744)	0.308	0.4	3.70±0.64	185	<i>HST</i>	45)
Cl 0016+16	0.546	0.6	8.5	370	WHT	23)
		0.4	3.74±1.28	90	<i>HST</i>	45)
Cl 0024+16	0.39	0.4	2.78±0.74	75	<i>HST</i>	45)
Cl 0054-27	0.56	0.4	3.42±1.28	200	<i>HST</i>	45)
Cl 0303+17	0.42	0.4	0.44±0.90	40	<i>HST</i>	45)
Cl 0412-65	0.51	0.4	0.50±0.82	35	<i>HST</i>	45)
Cl 0939+47	0.41	0.75(Mpc) 2 $(*)$	5	100	<i>HST</i>	25)
		0.4	1.46±0.82	60	<i>HST</i>	45)
Cl 1358+62	0.33	1	4.4	90±13	<i>HST</i>	46)
Cl 1455+22	0.259	0.45	3.6	540	WHT $iv)$	23)
Cl 1601+43	0.54	0.4	1.54±1.32	95	<i>HST</i>	45)
MS 1054-03	0.83	1	28±6	395±85	UH $v)$	24)
MS 1137+66	0.783	1	4.9±1.6	135±50	Keck II	38)
MS 1224+20	0.33	0.96	7.0	400	CFHT	22)
RXJ 1347-11	0.451	2	34±8	100±25	CTIO	50)
RXJ 1716+67	0.813	1	5.2±1.8	95±35	Keck II	38)
3C 295 (= Cl 1409+52)	0.46	0.4	4.70±0.76	165	<i>HST</i>	45)

Notes:

a) Redshift of the cluster.

b) Radius of the aperture in units of Mpc: (*) area of the observed field.

c) Projected cluster mass within the aperture of radius r in units of $10^{14}M_{\odot}$.

d) Mass-to-light ratio of the cluster in solar units.

e) Telescopes: i) Cerro Tololo Inter-American Observatory telescope; ii) Canada-France-Hawaii Telescope; iii) Hubble Space Telescope; iv) William Herschel Telescope; v) University of Hawaii telescope.

f) References

§6. Application to the cluster Abell 370

6.1. Background

Abell 370 is a very rich, distant cluster of galaxies at a redshift of 0.375, dominated by two bright cD galaxies. To this time, one GLA, several multiple images and a number of arclets have been observed in this cluster. The GLA was discovered by Soucail et al.⁵²⁾ and identified spectroscopically as the image of a background galaxy at a redshift of 0.724 lensed by Abell 370.⁵³⁾ Since the discovery of the GLA, the cluster has been the subject of extensive lensing studies and observations.^{10), 54) - 58)} Kneib et al.¹⁰⁾ investigated the mass distribution in Abell 370 on the basis of their excellent ground-based CCD image. Assuming that the GLA consists of three merging images, they constructed a detailed mass model based on two elliptical components associated with the two bright cD galaxies by fitting the model to the observed GLA and multiple images. Smail et al.⁵⁵⁾ discovered a radial-arc candidate in the *HST*/WFC1 image. Using the Kneib et al. model, they predicted its redshift to be 1.3 ± 0.2 . Ota et al.⁵⁷⁾ modeled the projected mass distribution in Abell 370 on the basis of the *ASCA* observation, assuming spherical mass profiles. They compared the radial profile of the projected mass inferred from X-ray analysis with that inferred from the Kneib et al. model based on strong lensing. The lensing mass interior to the GLA radius of $160h_{50}^{-1}$ kpc is about three times larger than the X-ray mass. They attributed the mass discrepancy for this cluster to the projection effect of substructures. Recently, AbdelSalam et al.⁵⁶⁾ developed a non-parametric method to reconstruct the cluster-mass distribution based on the observational constraints by strong lensing. They applied their non-parametric method to Abell 370; they divided the projected cluster mass into square pixels and searched for one of the solution for the mass distribution that follows galaxy light as closely as possible. From a visual inspection of the *HST*/WFC1 image,⁵⁵⁾ AbdelSalam et al. interpreted the GLA as a five-image system in contrast to the Kneib et al. model. Using the GLA, the multiple images and the radial arc, they obtained mass maps for Abell 370, which reveal an obvious bimodal feature in the mass distribution with the two mass peaks close to the two cD galaxies. However, the resulting two mass maxima were slightly closer to each other than the two cD galaxies. In addition, the southern mass clump was found to be more massive than the northern one, though the northern cD galaxy is brighter than the southern one, consistent with the Kneib et al. model. The interesting result obtained there is the presence of an extra substructure close to the two mass peaks, which does not follow the light. Bézecourt et al.⁵⁸⁾ improved the Kneib et al. model using the deep WFPC2 image. Detailed information concerning the GLA, multiple images and arclets placed strong constraints on the mass model consisting of the cluster- and galaxy-scale components.

In this section we present a non-parametric reconstruction of the mass distribution for Abell 370 based on weak-lensing analysis. In contrast to the mass reconstruction based on strong lensing as performed by Kneib et al., AbdelSalam et al. and Bézecourt et al., we do not use the information regarding the redshifts of the arcs: We make use of the information on the image shapes alone. Throughout this

section, we assume a matter-dominated Einstein-de Sitter universe with $\Omega_0 = 1$.

6.2. Observation and data reduction

The data for Abell 370 have been retrieved from the *HST* archive. The cluster Abell 370 was observed in December 1995 using the WFPC2 camera with the F675W filter (R_{675W}) on the *HST* (ID: 6003, P.I.: R. P. Saglia). The total exposure time is 5600 seconds. After STScI pipeline processing, the data were shifted and combined into the final frame to remove cosmic rays and hot pixels using the IRAF/STSDAS task CRREJ. We discarded the PC chip from our analysis because of its brighter isophotal limit, and thus the final frame consists of three WFPC chips. The side length of the data field is about $2'.5$, corresponding to $0.93h_{50}^{-1}$ Mpc at redshift $z_d = 0.375$. ($1''$ on the sky represents $6.2h_{50}^{-1}$ kpc.)

To construct a catalog of faint objects in this frame and measure the shape parameters (i.e., the center, the size and the complex ellipticity ϵ defined by Eq. (3.3)) for each object, we used the SExtractor package.⁵⁹⁾ We selected all objects with isophotal areas larger than 12 pixels (0.12 arcsec^2) above a detection threshold of $2\sigma/\text{pixel}$, corresponding to $\mu_{675W} = 24.5 \text{ mag arcsec}^{-2}$. The first and second brightness moments were computed for each object to determine the shape parameters. The faint and the bright magnitude limits were chosen so as to give reliable shape parameters. A catalog for arclet candidates was constructed with a total of 177 galaxies in a magnitude range $R_{675W} \in (23, 25)$.

As mentioned above, one GLA ($z = 0.724$) and one radial-arc candidate have been observed in the field of Abell 370. Through the detection process described above, the radial arc was identified as an object with $R_{675W} = 24.0$, and thus it was included in our catalog of faint galaxies with $R_{675W} \in (23, 25)$. On the other hand, the GLA was identified as a three-component image with $R_{675W} = 20.7, 20.6$ and 20.5 , so that this image system was excluded from our catalog of faint galaxies with $R_{675W} \in (23, 25)$. However, the GLA provides us with invaluable information on the mass distribution especially in the central region, and thus it will strongly constrain the cluster profile. Hence, we include this image system in our galaxy catalog. Thus the total number of the arclets contained in our galaxy catalog is

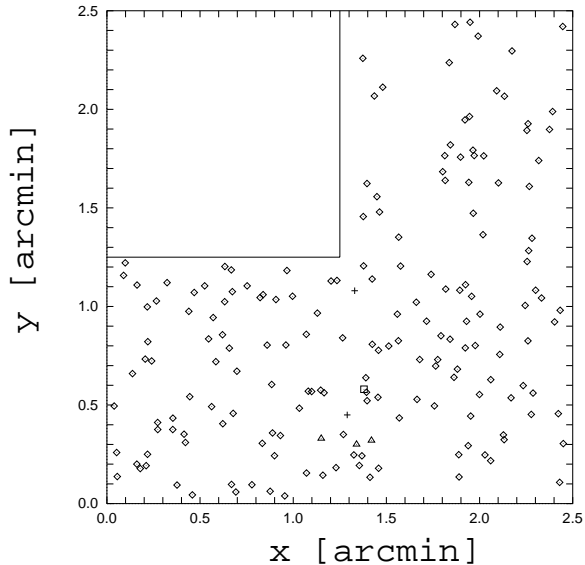


Fig. 2. Relative locations of the two cD galaxies and the image systems contained in our catalog of 180 galaxy images. North is to the top, and East is to the left. The positions of the two cD galaxies are marked with +. The positions of the giant luminous arc and the radial arc are marked with \triangle and \square , respectively. The positions of the other arclets are marked with \diamond .

$N_{\text{gal}} = 180$, corresponding to 38 galaxies arcmin^{-2} . In Fig. 2 we show the relative locations of the two cD galaxies and the image systems contained in our catalog of 180 galaxy images.

6.3. Shear field

In this subsection we describe the shear analysis of Abell 370. First, we divide the CCD-data field consisting of three WFC chips into two rectangular fields A and B; field A with a side length of about $2'.5 \times 1'.25$ consisting of the lower-left and the lower-right WFC chips, and field B with a side length of about $1'.25 \times 2'.5$ consisting of the lower-right and upper-right WFC chips. Both the cD galaxies are located at the left edge of the lower-right WFC chip (see Fig. 2), and thus both the fields A and B contain them. For field A, the number of the galaxies contained in our catalog is 142, corresponding to a galaxy-number density of 46 arcmin^{-2} . On the other hand, for field B, the number of galaxies contained in our catalog is 107, and the corresponding galaxy-number density is 35 arcmin^{-2} , which is much smaller than a typical galaxy-number density of $\sim 50 \text{ galaxies arcmin}^{-2}$ in a weak-lensing analysis. This small number density is ascribed to the small number of faint galaxies detected in the upper-right WFC frame from our analysis (38 galaxies in this frame; see Fig. 2).

Next, we introduce a rectangular grid with a constant grid separation of $0'.083$ ($31h_{50}^{-1} \text{ kpc}$) for each field: field A with 30×15 grid points, and field B with 15×30 grid points. In order to reduce the noise due to the intrinsic ellipticities of the background galaxies, we calculate the local mean image ellipticity $\bar{\epsilon}(\vec{\theta}_{ij})$ at each grid point $\vec{\theta}_{ij}$ from the image ellipticity $\epsilon(\vec{\theta}_k)$ of the k -th galaxy at angular position $\vec{\theta}_k$ ($k = 1, 2, \dots, N_{\text{gal}}$; $N_{\text{gal}} = 180$) (see Eqs. (3.15) and (3.16)). Here we employ

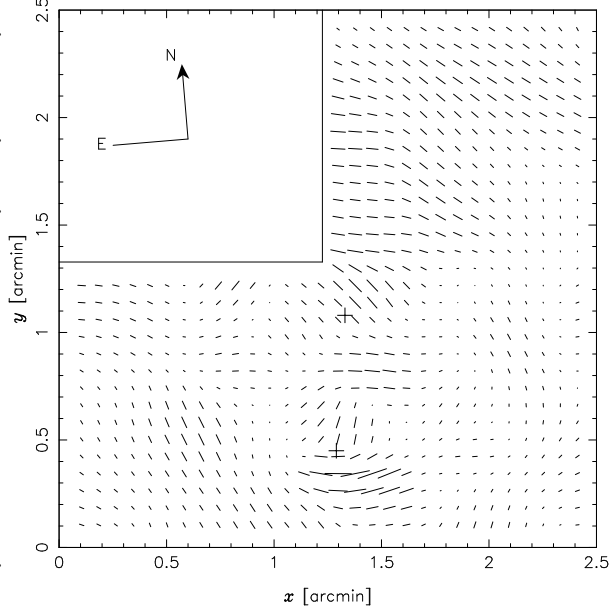


Fig. 3. The shear field obtained from 180 galaxy images taken with the *HST*/WFPC2. The orientation and the length of a vector indicate the orientation ϕ and the absolute value $|\bar{\epsilon}|$ of the locally-averaged image ellipticity $\bar{\epsilon} = |\bar{\epsilon}| e^{2i\phi}$, respectively. The case $|\bar{\epsilon}| = 1$ (i.e., vanishing axis ratio) corresponds to a vector of length $0'.3$. We adopt an optimal smoothing length $\Delta\theta$ depending on the distance from the positions $\vec{\theta}_N$ and $\vec{\theta}_S$ of the northern and the southern cD galaxies, respectively; $\vec{\theta}_N = (1'.33, 1'.08)$ and $\vec{\theta}_S = (1'.29, 0'.45)$. The smoothing length $\Delta\theta$ ranges from $\sim 0'.1$ (37 kpc) to $\sim 0'.3$ (112 kpc), depending on the grid position; $1'$ corresponds to 0.37 Mpc at the cluster redshift $z_d = 0.375$ for $H_0 = 50 \text{ km s}^{-1} \text{ Mpc}^{-1}$ and an Einstein-de Sitter universe. The positions of the two cD galaxies are marked with +.

an optimal smoothing procedure; we adopt an optimal smoothing length $\Delta\theta(\vec{\theta}_{ij})$ in Eq. (3-16) depending on the grid position $\vec{\theta}_{ij}$ such that

$$\Delta\theta(\vec{\theta}_{ij}) = \min(0.12|\vec{\theta}_{ij} - \vec{\theta}_N| + \Delta\theta_0, 0.12|\vec{\theta}_{ij} - \vec{\theta}_S| + \Delta\theta_0) \text{ arcmin}, \quad (6-1)$$

with constant smoothing length $\Delta\theta_0 = 0'.1$, where $\vec{\theta}_N$ and $\vec{\theta}_S$ are the angular positions of the northern and the southern cD galaxies, respectively; $\vec{\theta}_N = (1'.33, 1'.08)$ and $\vec{\theta}_S = (1'.29, 0'.45)$ in our coordinate system. Thus the smoothing length $\Delta\theta(\vec{\theta}_{ij})$ at grid position $\vec{\theta}_{ij}$ ranges from $\sim 0'.1$ ($37h_{50}^{-1}$ kpc) to $\sim 0'.3$ ($112h_{50}^{-1}$ kpc), depending on the distance from the positions $\vec{\theta}_N$ and $\vec{\theta}_S$ of the two cD galaxies.

Figure 3 displays the resulting map of the locally-averaged image ellipticities $\bar{e} = |\bar{e}| e^{2i\phi}$ obtained using 180 arclet candidates. The orientation of a vector indicates the direction ϕ of the shear, and the length of a vector is proportional to the strength of the shear. A coherent shear pattern induced by the gravitational field of the cluster is clearly visible.

6.4. Mass reconstruction

Using the smoothed image-ellipticity field $\bar{e}(\vec{\theta}_{ij})$ obtained from our galaxy catalog, we reconstruct the mass distribution of the cluster Abell 370. To take into account (1) the strong-lensing features in the cluster field, (2) the fairly high redshift of the cluster ($z_d = 0.375$) and (3) the small field-of-view of the *HST*/WFPC2 field, we follow the generalized mass-reconstruction scheme³²⁾ based on the finite-field inversion derived by Seitz and Schneider²⁰⁾ (see § 4.3 and 4.4).

Because of the irregular shape of the WFC field, we separately reconstruct the two-dimensional convergence fields $\kappa_{\infty,A}(\vec{\theta}_{ij})$ and $\kappa_{\infty,B}(\vec{\theta}_{ij})$ on two rectangular fields A and B, respectively, as done in Ref. 25). Since a mass reconstruction with the finite-field formula (4-31) yields a constant $\bar{\kappa}_{\infty}$, which represents the average of κ_{∞} over the data field, we have two free constants in our reconstruction, $\bar{\kappa}_{\infty,A}$ for field A and $\bar{\kappa}_{\infty,B}$ for field B. One of the two constants can be used to join the two reconstructions, and the residual constant can be used to normalize the cluster mass. The procedure to determine the two constants and to join the two independent reconstructions is described in § 6.5.

Moreover, we must know the redshift distribution of the galaxy population in the mass reconstruction (see § 4.4). However, the redshift distribution of faint galaxies with $R_{675W} \in (23, 25)$ is uncertain, so that we adopt a parameterized redshift

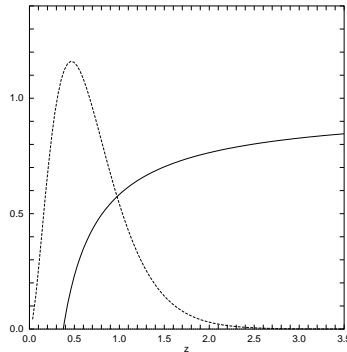


Fig. 4. The solid line indicates the relative lensing strength $w(z)$ defined by Eq. (4-37) for the cluster redshift $z_d = 0.375$. The dashed line indicates the assumed redshift distribution $p_z(z)$ of background galaxies defined by Eq. (6-2) for $\beta = 1$ and $\langle z \rangle = 3z_0 = 0.7$.

distribution $p_z(z)$ of field galaxies of the form^{25),60)}

$$p_z(z) = \frac{\beta z^2}{\Gamma(3/\beta)z_0^3} \exp\left(-(z/z_0)^\beta\right), \quad (6.2)$$

with mean redshift $\langle z \rangle = z_0\Gamma(4/\beta)/\Gamma(3/\beta)$. We use the redshift distribution (6.2) with $\beta = 1$ and $\langle z \rangle = 3z_0 = 0.7$ in our analysis. In Fig. 4 we show this redshift distribution $p_z(z)$ for $\beta = 1$ and $\langle z \rangle = 3z_0 = 0.7$ and the relative lensing strength $w(z)$ defined by Eq. (4.37) for the cluster redshift $z_d = 0.375$.

6.5. Results

Figure 5 displays the two-dimensional κ_∞ -field for Abell 370 obtained using our galaxy sample and the redshift distribution (6.2) with $\beta = 1$ and $\langle z \rangle = 0.7$. In Fig. 6 we show the corresponding contour map of the κ_∞ -reconstruction.

In the reconstruction, we have determined the two constants $\bar{\kappa}_{\infty,A}$ and $\bar{\kappa}_{\infty,B}$ in the following way: (i) We employ the well-constrained mass model constructed by Kneib et al.¹⁰⁾ using the GLA and multiple images. The mean convergence within field A is calculated to be 0.832 using this model. (ii) Adopting this value for $\bar{\kappa}_{\infty,A}$, we determine $\bar{\kappa}_{\infty,B}$ such that the averages of $\kappa_{\infty,A}(\vec{\theta}_{ij})$ and $\kappa_{\infty,B}(\vec{\theta}_{ij})$ within the overlapping region of the fields A and B are the same. The mean convergence in this overlapping region is 0.786, and the mean convergence in field B is 0.764. (iii) Joining together the two independent κ_∞ -reconstructions along the diagonal of the overlapping quadrangle, we obtain the resulting convergence map $\kappa_\infty(\vec{\theta}_{ij})$, as was done in Ref 25). It can be seen in Figs. 5 and 6 that the discontinuity across this diagonal in our reconstruction is remarkably small. From the resulting $\bar{\kappa}_\infty$ -map, the mean convergence $\bar{\kappa}_\infty$ inside the observed field of $0.65h_{50}^{-2}$ Mpc² is calculated to be 0.811, yielding a total mass in this field of $M \simeq 8.0 \times 10^{14}h_{50}^{-1}M_\odot$.

The main features in the resulting mass map are summarized as follows:

- (1) Our mass reconstruction exhibits a clear bimodal feature in the central region where the two cD galaxies are located. The locations of the two mass maxima ($\kappa_\infty = 1.14$) in the mass map coincide well with those of the two cD galaxies: The location of the northern mass clump is in good agreement with that of the northern cD galaxy, while the southern mass clump is located slightly offset from the southern cD galaxy, but is consistent with the location of the southern cD galaxy within a smoothing scale and a grid separation of $\sim 0'.1$ ($37h_{50}^{-1}$ kpc).
- (2) The reconstructed mass map reveals a likely substructure (marked with \star in Fig. 6) located about $0'.3$ (110 kpc) to the left relative to the center of the two cD galaxies.
- (3) An increase of κ_∞ toward the lower-left corner in the lower-left quadrangle is visible.
- (4) The cluster-mass distribution is super-critical especially in the innermost region where the two cD galaxies and hence the two mass clumps lie. To be more precise, this distribution is super-critical for sources at an infinite or a sufficiently high redshift. However, the reconstructed mass distribution is sub-critical for the GLA at a redshift of 0.724; $w(z) = 0.45$ for $z = 0.724$ (see Eq. (4.37)).

Finally, it should be mentioned that these main features are insensitive to the as-

sumed redshift distribution $p_z(z)$ of field galaxies and the smoothing procedure which is needed in calculating the smoothed image ellipticity $\bar{\epsilon}$.

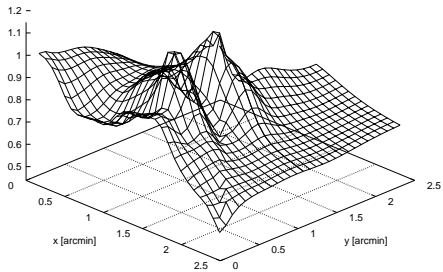


Fig. 5. The κ_∞ -distribution for the cluster Abell 370 ($z_d = 0.375$) reconstructed from the shear field shown in Fig. 3. The side length is about 2.5 corresponding to 0.93 Mpc at the cluster redshift $z_d = 0.375$ for $H_0 = 50 \text{ km s}^{-1} \text{ Mpc}^{-1}$ and an Einstein-de Sitter universe. In the reconstruction we used the redshift distribution $p_z(z)$ defined by Eq. (6.2) with $\beta = 1$ and $\langle z \rangle = 0.7$. Our reconstruction exhibits a clear bimodal feature in the central region of the cluster. A likely substructure is visible near to the two cD galaxies.

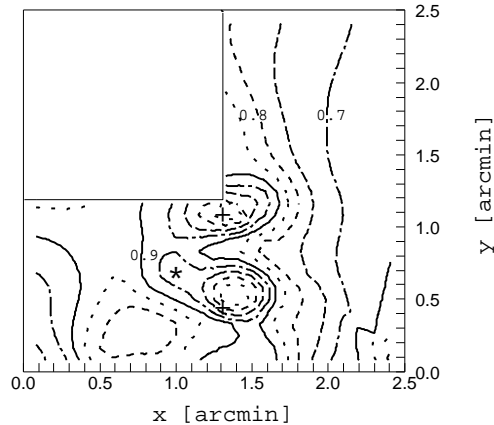


Fig. 6. Contour plot of the resulting κ_∞ -distribution shown in Fig. 5. The positions of the two cD galaxies are marked with +. The position of the northern mass clump agrees well with that of the northern cD galaxy. The southern mass clump is located slightly offset from the southern cD galaxy. The position of the extra substructure is marked with *. The contours are stepped in units of 0.05.

6.6. Discussion

Focusing on the morphology of the cluster, we have investigated the mass distribution of Abell 370 on the basis of weak lensing. We reconstructed the two-dimensional mass distribution of Abell 370 from the ellipticities of the faint galaxy images obtained using the *HST*/WFPC2 data. In the reconstruction, we used a total of 180 galaxy images consisting of 176 arclets, a radial arc and a GLA as a three-image system. Taking account of the small field-of-view of the data field, the strong-lensing features in the cluster and the fairly high redshift ($z_d = 0.375$) of the cluster, we applied the generalized mass-reconstruction scheme described in Section 4.4. From the shear field of galaxy images, the mass distribution of the cluster was determined up to a one-parameter family of the global transformations which leaves the observed image distortions invariant. We employed the well-constrained mass model by Kneib et al.¹⁰⁾ based on strong lensing in order to infer the mass in the central region, from which we broke the mass degeneracy. Assuming a mean redshift of $\langle z \rangle = 0.7$ for the field galaxies with $R_{675W} \in (23, 25)$, we have estimated the cluster mass within our data field of $0.65h_{50}^{-2} \text{ Mpc}^2$ to be $\sim 8 \times 10^{14} h_{50}^{-1} M_\odot$.

The resulting mass map also provides valuable information regarding the distribution of dark matter. Our direct mass reconstruction exhibits a clear bimodal

feature associated with the two cD galaxies. Furthermore, our mass reconstruction reveals some other features: An extra substructure in the vicinity of the two cD galaxies and a mass condensation toward the lower-left boundary are visible. However, since the accuracy of mass reconstructions tends to be worse near the boundary of the data field, the mass increase toward the boundary corner might be due to the systematic boundary effect and/or the fact that fewer galaxy images are used at the boundary corner in averaging image ellipticities. In addition, since the galaxy-number density in the upper-right WFC is quite small (see Fig. 2), the reconstructed mass distribution may be different from the actual one in that region. The resulting mass distribution of the cluster is found to be super-critical for sources at a sufficiently-high redshift but sub-critical for the GLA at a redshift of 0.724. This result can be attributed to the smoothing procedure which is needed to reduce the noise due to the intrinsic ellipticities of background galaxies: Although the global mass distribution of a cluster can be obtained by locally averaging the galaxy-image ellipticities, such averaging will smooth out the galaxy-scale structure in the cluster. As a result, the reconstructed mass distribution will tend to be flatter than the original one. Hence, strong-lensing effects such as GLAs and multiple images should be combined with weak-lensing analysis in order to reproduce the mass distribution in the innermost region of the cluster. Alternatively, the galaxy-galaxy lensing analysis can probe the mass distributions in clusters on galaxy scales.^{61) - 64)}

Finally, we should comment on our treatment of arcs: a GLA and a radial arc. In general, strong-lensing features such as GLAs and radial arcs strongly constrain the mass distribution of the deflector, especially in its central region where they are located. In fact, the reconstruction without taking into account the arcs exhibits a bimodal feature, but the density of the southern peak turns out to be lower than that of the northern peak. Thus the comparison between the resulting mass maps with and without the arcs reveals a remarkable influence of the arcs on the reconstructed mass distribution.

§7. Summary

Weakly- and coherently-distorted images of background galaxies induced by intervening galaxy clusters can be used to determine the mass distributions in the clusters on scales ~ 1 Mpc. Kaiser and Squires have derived an exact expression for the projected-mass distribution of the lensing cluster in terms of the gravitational shear which can be measured from the observed galaxy images. The original Kaiser and Squires technique was then generalized to include the strong-lensing regime and to optimize real observations.

To this time, these direct mass-reconstruction methods based on shear analysis have been applied to a number of clusters. Now, the weak-distortion fields of galaxy images have become one of the most promising tools to probe the mass distribution of clusters. Moreover, the weak-shear field also provides a clue to the distant population of faint background galaxies: The weak-lensing analysis for a high-redshift cluster combined with a strongly-constrained mass model can place strong constraints on the redshift distribution of a distant population since the lensing strength depends

quite strongly on the source redshift through the distance ratio D_{ds}/D_s (or $w(z)$) for a high-redshift cluster. The detection of significant lensing signals for some high-redshift clusters ($z_d \sim 0.8$) indicates that a substantial part of the faint galaxy population must lie at sufficiently high redshifts ($z > 1$).

In this paper we have applied a direct mass-reconstruction method to the cluster Abell 370 at a redshift of $z_d = 0.375$ observed with the *HST*/WFPC2. Despite the small field-of-view and the irregular shape of the data field, our direct mass reconstruction of Abell 370 demonstrates the feasibility of weak-lensing analysis based on the shear field. However, there remains an uncertainty concerning the mass normalization of the cluster. Such an uncertainty occurs if the mass distribution of the cluster extends beyond the observed data field, in which case we cannot determine the cluster-mass distribution directly from the observed image distortions. We expect that such a difficulty will be overcome by 8-10 m class telescopes with a wide field-of-view, such as the 8.3 m Subaru telescope with Suprime-Cam.

Acknowledgements

We are very grateful to P. Schneider for informing us of his unpublished works and for his valuable suggestions. We also wish to thank M. Hattori for fruitful discussions concerning previous works on the cluster Abell 370. Part of this work is based on an observation with the NASA/ESA *Hubble Space Telescope*, obtained from the data archive at the Space Telescope Science Institute (STScI). STScI is operated by the Association of Universities for Research in Astronomy, Inc. under the NASA contract NAS 5-26555.

References

- 1) J. P. Henry and K. A. Arnaud, *Astrophys. J.* **372** (1991), 410.
- 2) D. O. Richstone, A. Loeb and E. L. Turner, *Astrophys. J.* **393** (1992), 477.
- 3) N. A. Bahcall, L. Lubin and V. Dorman, *Astrophys. J.* **447** (1995), L81.
- 4) J. Binney and S. Tremaine, *Galactic Dynamics* (Princeton: University Press, 1987).
- 5) C. L. Sarazin, *Rev. Mod. Phys.* **58** (1986), 1.
- 6) R. Webster, *Mon. Not. R. Astron. Soc.* **213** (1985), 871.
- 7) J. Tyson, F. Valdes and R. A. Wenk, *Astrophys. J.* **349** (1990), L1.
- 8) C. A. Kochanek, *Mon. Not. R. Astron. Soc.* **247** (1990), 135.
- 9) J. Miralda-Escudé, *Astrophys. J.* **370** (1991), 1.
- 10) J.-P. Kneib, Y. Mellier, B. Fort and G. Mathez, *Astron. Astrophys.* **273** (1993), 367.
- 11) X. P. Wu and S. Mao, *Astrophys. J.* **463** (1996), 404.
- 12) T. Futamase, M. Hattori and T. Hamana, *Astrophys. J.* **598** (1998), L47.
- 13) H. Bonnet, Y. Mellier and B. Fort, *Astrophys. J.* **427** (1994), L83.
- 14) N. Kaiser and G. Squires, *Astrophys. J.* **404** (1993), 441.
- 15) N. Kaiser, *Astrophys. J.* **439** (1995), L1.
- 16) P. Schneider and C. Seitz, *Astron. Astrophys.* **294** (1995), 411.
- 17) C. Seitz and P. Schneider, *Astron. Astrophys.* **297** (1995), 287.
- 18) M. Bartelmann, *Astron. Astrophys.* **303** (1995), 643.
- 19) P. Schneider, *Astron. Astrophys.* **302** (1995), 639.
- 20) S. Seitz and P. Schneider, *Astron. Astrophys.* **305** (1996), 383.
- 21) G. Squires and N. Kaiser, *Astrophys. J.* **473** (1996), 65.
- 22) G. G. Fahlmann, N. Kaiser, G. Squires and D. Woods, *Astrophys. J.* **437** (1994), 56.
- 23) I. Smail, R. S. Ellis, M. J. Fitchett and A. C. Edge, *Mon. Not. R. Astron. Soc.* **273** (1995), 277.

- 24) G. Luppino and N. Kaiser, *Astrophys. J.* **475** (1997), 20.
- 25) C. Seitz, J.-P. Kneib, P. Schneider and S. Seitz, *Astron. Astrophys.* **314** (1996), 707.
- 26) B. Fort and Y. Mellier, *Astron. Astrophys. Rev.* **5** (1994), 239.
- 27) Y. Mellier, L. Van Waerbeke, F. Bernardeau and B. Fort, Preprint astro-ph/9609197.
- 28) P. Schneider and M. Bartelmann, private communication.
- 29) P. Schneider, J. Ehlers and E. E. Falco, *Gravitational Lenses* (Geidelberg: Springer, 1992).
- 30) R. D. Blandford and R. Narayan, *Ann. Rev. Astron. Astrophys.* **30** (1992), 311.
- 31) R. Narayan and M. Bartelmann, Preprint astro-ph/9606001.
- 32) C. Seitz and P. Schneider, *Astron. Astrophys.* **318** (1997), 687.
- 33) T. G. Brainerd, I. Smail and J. R. Mould, *Mon. Not. R. Astron. Soc.* **275** (1995), 781.
- 34) M. Bartelmann and R. Narayan, *Astrophys. J.* **451** (1995), 60.
- 35) M. Lombardi and G. Bertin, *Astron. Astrophys.* **335** (1998), 1.
- 36) P. Schneider and M. Bartelmann, *Mon. Not. R. Astron. Soc.* **286** (1997), 696.
- 37) I. Smail, R. S. Ellis and M. J. Fitchett, *Mon. Not. R. Astron. Soc.* **270** (1994), 245.
- 38) D. Clowe, N. Kaiser, G. Luppino, J. P. Henry and I. M. Gioia, *Astrophys. J.* **497** (1998), L61.
- 39) S. Schindler and J. Wambsgans, *Astron. Astrophys.* **313** (1996), 113.
- 40) P. Fischer, G. Bernstein, G. Rhee and J. A. Tyson, *Astron. J.* **113** (1997), 521.
- 41) G. Squires, N. Kaiser, A. Babul, G. Fahlman, D. Woods, D. M. Neumann and H. Böhringer, *Astrophys. J.* **461** (1996), 572.
- 42) G. Squires, N. Kaiser, G. Fahlman, A. Babul and D. Woods, *Astrophys. J.* **469** (1996), 73.
- 43) G. Squires, D. M. Neumann, N. Kaiser, M. Arnaud, A. Babul, H. Böhringer, G. Gahlman and D. Woods, *Astrophys. J.* **482** (1997), 648.
- 44) S. W. Allen, *Mon. Not. R. Astron. Soc.* **296** (1998), 392.
- 45) I. Smail, R. S. Ellis, A. Dressler, W. J. Couch, A. Oemler, R. M. Sharples and H. Butcher, *Astrophys. J.* **497** (1997), 70.
- 46) H. Hoekstra, M. Franx, K. Kuijken and G. Squires, *Astrophys. J.* **504** (1998), 636.
- 47) <http://indus.astron.s.u-tokyo.ac.jp/works/suprime/>.
- 48) N. Kaiser, G. Wilson, G. Luppino, L. Kofman, M. Metzger and H. Dahle, Preprint astro-ph/9809268.
- 49) J. A. Tyson and P. Fischer, *Astrophys. J.* **446** (1995), L55.
- 50) P. Fisher and J. A. Tyson, *Astron. J.* **114** (1997), 14.
- 51) X.-P. Wu and L.-Z. Fang, *Astrophys. J.* **483** (1997), 62.
- 52) G. Soucail, B. Fort, Y. Mellier and J.-P. Picat, *Astron. Astrophys.* **172** (1987), L14.
- 53) G. Soucail, Y. Mellier, B. Fort, G. Mathez and M. Cailoux, *Astron. Astrophys.* **191** (1988), L19.
- 54) Y. Mellier, G. Soucail, B. Fort and G. Mathez, *Astron. Astrophys.* **199** (1998), 13.
- 55) I. Smail, A. Dressler, J.-P. Kneib, R. S. Ellis, W. Couch, R. Sharples and A. Oemler, *Astrophys. J.* **469** (1996), 508.
- 56) H. M. AbdelSalam, P. Saha and L. L. R. Williams, *Mon. Not. R. Astron. Soc.* **294** (1998), 734.
- 57) N. Ota, K. Mitsuda and Y. Fukazawa, *Astrophys. J.* **495** (1998), 170.
- 58) J. Bézecourt, J.-P. Kneib, G. Soucail and T. M. D. Ebbels, Preprint astro-ph/9810199.
- 59) E. Bertin and S. Arnouts, *Astron. Astrophys. Suppl.* **117** (1996), 393.
- 60) T. G. Brainerd, R. D. Blandford and I. Smail, *Astrophys. J.* **466** (1996), 623.
- 61) P. Natarajan and J.-P. Kneib, *Mon. Not. R. Astron. Soc.* **287** (1997), 833.
- 62) P. Natarajan, J.-P. Kneib, I. Smail and R. S. Ellis, *Astrophys. J.* **499** (1998), 600.
- 63) B. Geiger and P. Schneider, *Mon. Not. R. Astron. Soc.* **295** (1998), 497.
- 64) B. Geiger and P. Schneider, *Mon. Not. R. Astron. Soc.* **302** (1999), 118.